Estimating depth to bedrock in weathered terrains using ground-penetrating radar: a case study in the Adelaide Hills

Thesis submitted in accordance with the requirements of the University of Adelaide for an Honours Degree in Geophysics

Dylan Cremasco

November 2013

THE UNIVERSITY of ADELAIDE

TITLE

Estimating depth to bedrock in weathered terrains using ground-penetrating radar: a case study in the Adelaide Hills

RUNNING TITLE

Bedrock depth estimation using ground-penetrating radar

ABSTRACT

Ground-penetrating radar (GPR) is a geophysical technique that is commonly applied to a variety of subsurface investigations, with the capability to determine depth to bedrock under favourable soil conditions. This study was conducted at three different physiographic regions that represent typical terrains in the Adelaide Hills. At each site, GPR surveys were conducted along traverses using 100, 250, 500 and 800 MHz antennae. A drilling program was conducted concurrently with the GPR survey to provide baseline bedrock depths for comparison. Electrical resistivity and electromagnetic surveys were also conducted along each traverse to determine subsurface conductivity and secondary bedrock depth estimates. The GPR results for all antennae were compared to determine the frequency that provided the best depth estimation. Rapid attenuation of GPR signal at all frequencies was observed, resulting in shallower than expected investigation depths. At two of the sites, GPR signal penetration depth was increased in areas that were highly resistive. The 800 MHz antennae displayed the highest resolution of estimated bedrock contacts in these resistive areas, and were subsequently compared to drill refusal depths using a paired *t* test. GPR estimation depths and drill refusal in electrically resistive areas strongly correlated at two of the sites, while the third site showed no correlation. Across all three transects bedrock depths were underestimated by 74% on average. This underestimation is attributed to signal attenuation, which appears to be caused by a combination of increased conductivity, clay content and the presence of iron oxides in the soil profile. Without further investigation it is difficult to quantify these factors on attenuation in the area. The results of this study suggest that GPR surveys are not suitable for bedrock depth estimation in Adelaide Hills-type terrains.

KEYWORDS

Ground-penetrating radar, bedrock depth, Adelaide Hills, site productivity, soil profile, attenuation

TABLE OF CONTENTS

LIST OF FIGURES

LIST OF TABLES

This page is intentionally blank

1. INTRODUCTION

The depth to bedrock from the ground surface, and therefore the thickness of the overlying soil, strongly correlates with the distribution of horizons within a soil profile. Soil physical and chemical properties, such as groundwater interactions, sub-soil water movement, water storage and nutrient availability are all factors that are controlled by the horizon distribution and thickness (Sucre *et al.* 2010). The overall productivity of a site is regulated by these soil properties (Wilford & Thomas 2012). Typically, a soil profile includes the A, B and C horizons (Fitzpatrick 1988). Moderately weathered bedrock below the C horizon is recognised as the R horizon (McDonald & Isbell 2009). The depth to this R horizon is considered in soil science to represent the contact point between the soil profile and underlying bedrock (Fitzpatrick 1988, McDonald & Isbell 2009). Determining the depth to the R horizon can provide essential information about a soils properties when investigating potential land uses (Sucre *et al.* 2010, Wilford & Thomas 2012).

Depth to bedrock is commonly measured by traditional mechanical methods. These ground truthing practises include augering, coring and excavation (Collins & Doolittle 1987). All of these techniques are time consuming, expensive and often result in high levels of soil disturbance (Collins & Doolittle 1987). Ideally, a cheaper, more accessible and less destructive ground truthing method is required. Determining depth to bedrock using shallow geophysical techniques has been documented in a variety of terrains (Davis & Annan 1989, Jol & Smith 1991, Wightman *et al.* 1992, Triantafilis & Buchanan 2009, Sucre *et al.* 2010, Coulouma *et al.* 2011). The use of these techniques within the erosional landscapes of the Adelaide Hills for bedrock depth estimation has

not been previously investigated. Due to the varying limitations and conditional requirements of geophysical equipment, the effectiveness of applied methods will vary depending on the style of landscape and the underlying soil profile (Samouelian *et al.* 2004, Sucre *et al.* 2010). Previous work suggests that ground-penetrating radar (GPR) holds the potential to accurately estimate depth to bedrock in complex weathered terrains (Doolittle & Collins 1995), such as those seen in the Adelaide Hills region. The speed, cost and ease of data acquisition make GPR an attractive method for bedrock depth estimation. The use of GPR under favourable conditions has been found to reduce field cost by up to 70%, and increase efficiency by 210% (Doolittle & Collins 1995).

The successful application of GPR is dependent on the physical and chemical characteristics of the subsurface, such as bulk conductivity and presence of clay (Olhoeft 1986, Du & Rummel 1994, Doolittle & Collins 1995, Reynolds 1997). These factors control the overall quality of signal transmission and reflection (Saarenketo 1998). Optimal subsurface conditions for GPR include electrically resistive sands, gravels and clastic sediments (Jol & Smith 1991, Jol & Bristow 2003). Incompatible soils result in the loss of transmitted GPR signal (Olhoeft 1986, Doolittle & Collins 1995). This signal loss, called attenuation, minimises the total depth of GPR survey investigation (Reynolds 1997, Annan 2005). Sucre *et al.* (2010) investigated the use of GPR for bedrock depth estimation within the Southern Appalachian Mountains, concluding it to be an effective technique, though highly dependent on the electrical conductivity of the overlying soils. GPR surveys have been conducted for a wide range of applications in Australia, with only a limited number of these regarded as being successful (Griffin & Pippet 2002). Soils occurring within Australia tend to be more

conductive than those found in other countries, reducing the effectiveness of GPR surveys (Griffin & Pippet 2002, McDonald & Isbell 2009). Taking these findings into account, other forms of geophysical investigation should be considered to provide additional subsurface information in any areas in which the GPR signal becomes attenuated. Two common shallow ground geophysical techniques for measuring soil conductivity include electrical resistivity surveys and electromagnetic (EM) surveys (Kearey *et al.* 2002, Fitterman & Labson 2005, Zonge *et al.* 2005). High soil conductivity readings from these techniques can potentially provide an explanation for unexpected GPR signal attenuation.

Electrical resistivity techniques aim to determine the resistivity of the surrounding soil volume (Samouelian *et al.* 2004, Zonge *et al.* 2005). Electrical resistivity of soil volumes can be considered as a proxy for the variability of a variety of soil properties; such as structure and water content (Banton *et al.* 1997, Samouelian *et al.* 2004). The use of electrical resistivity surveying for bedrock depth estimation is greatly influenced by the contrast in electrical resistivity between the soils and underlying bedrock (Coulouma *et al.* 2010, Coulouma *et al.* 2011). Low electrical resistivity contrast between the soil and underlying bedrock results in a low resolution contact point on the resistivity imaging, providing less accurate bedrock depth estimations (Banton *et al.* 1997, Coulouma *et al.* 2011). The ability of these systems to provide useful information on the subsurface conductivity distribution, while providing an alternate method of bedrock depth detection, makes them a desirable instrument to include in this survey. EM survey methods are commonly used to map near-surface geology by tracing variations in the electrical conductivity properties of underlying rocks and soils

(Doolittle *et al.* 1994, Fitterman & Labson 2005). Similar to electrical resistivity, electromagnetic variations are generally controlled by soil and rock structure, porosity, clay content, groundwater salt content and water saturation (McNeill 1990, Doolittle *et al.* 1994). EM surveys are commonly employed for groundwater, salinity and clay profiling (McNiell 1980, Doolittle *et al.* 1994), though the potential of mapping sedimentary stratigraphy and bedrock contacts has been investigated. Electromagnetic response analysis for a multi-layered earth model conducted by McNiell (1980) found shallow terrain conductivity meters, like the Geonics EM-31 system, to be theoretically capable of mapping soil-bedrock contacts when high conductivity contrasts are present at the interface between the two materials. Frequency domain electromagnetic surveys (FDEM) conducted by Wightman *et al.* (1992) showed highly conductive shale bedrock to be modelled by the technique through up to 15 m of overburden. FDEM surveys conducted by Triantafilis and Buchanan (2009) along the Darling River valley were used for the purpose of mapping near surface and sub-surface stratigraphic units. The results were used to interpret soil clay content, cation exchange capacity and soil electrical conductivity. These estimations can provide useful information for this study, as such properties often are associated with the soil profile thickness and type of bedrock present (Wightman *et al.* 1992).

This work evaluates the suitability of GPR to provide depth to bedrock measurements within the complex and weathered terrains of the Adelaide Hills. Study sites were chosen within the Mount Crawford Forestry Reserve, South Australia. In order to test the versatility of the approach across variable terrains and parent materials, survey lines were selected within three contrasting physiographic regions. Ground truthing data were

also collected by using traditional drilling methods for direct comparison to GPR survey results. EM and electrical resistivity survey results are also compared to GPR and ground truthing data. By analysing these comparisons, this study aims to provide insight into the ability of GPR to estimate depth to bedrock in this type of terrain.

2. GEOLOGICAL SETTING

2.1 Regional tectonic history

The Mount Crawford Forestry Reserve is a grouping of several native and plantation forests surrounding the Mount Crawford area, located within the central Mount Lofty Ranges in South Australia. Tokarev (2005) identifies the Mount Lofty Ranges to be the result of a complex neotectonic deformational history in the region; specifically an extensional regime (Middle Eocene to Middle Miocene), a transitional stage (Late Miocene to Early Pleistocene) and a compressional regime (Early Pleistocene to present). Crustal segmentation in the region during the later stages of the Eocene resulted in the subsidence of the surrounding St. Vincent and Western Murray Basins (Sandiford 2002, Tokarev 2005). The central palaeoplain between the subsiding basins shaped what would eventually become the Mount Lofty Ranges (Benbow *et al.* 1995). The influence of a compressional neotectonic regime caused the formation of steep reverse faulting on either side of the palaeoplain (Tokarev 2005). These fault scarps align along a roughly north-south line and persist throughout the length of the ranges (Bourman & Lindsay 1989, Sandiford 2002). Uplift of the central palaeoplain caused by the compressional regime lead to the formation of the Mount Lofty Ranges (Sandiford 2002, Tokarev & Gostin 2003). The uplift of the Ranges primarily occurred during the

Pleistocene, with present day in-situ stress measurements and seismic activity indicating the continuing uplift of the area (Sandiford 2002, Tokarev 2005).

2.2 Local geology

The Palaeoproterozoic Barossa Complex of the Houghton Inlier forms the basement underneath the Mount Lofty Ranges (Preiss 1987). The basement is unconformably overlain by Adelaidean metasediments, forming an approximately 7 km thick cover over the region (Preiss 1987). During the Cambrian Delamerian Orogeny, the Adelaidean sediments were metamorphosed to greenschist facies (Preiss *et al.* 2008). The Warren Inlier, an anticlinal core of pre-Adelaidean basement, is located within the metamorphosed sediments (Preiss *et al.* 2008). The Aldgate sandstone that overlies the Mount Crawford area passes eastward into the Springfield Shear Zone (Preiss 1987). Structurally overlying the Aldgate Sandstone is the highly deformed micaceous feldspathic meta-siltstones and meta-sandstones of the Cambrian Kanmantoo Group (Preiss *et al.* 2008, Wilford & Thomas 2012). Two differing perspectives on the source of the highly deformed micaceous schist have been theorised: Conor (1984) described polyphase deformation of Adelaidean metasediments to be the source. Conversely, Townsend (1984) identified similarities in the mica schist to that of migmatic schist from the pre-Adelaidean Warren Inlier, and suggested the source to be a sheet of pre-Adelaidean basement that had been thrust into the metasediments. The exposed micaceous schist at Mount Crawford is host to migmatite and the related Mount Crawford Granite Gneiss (Preiss *et al.* 2008). High grade basement units and pre to syn-tectonic granitiod intrusive bodies are also observed in the area (Daily *et al.* 1976).

2.3 Study area

The study area within the Mount Crawford Forestry Reserve shows varying landforms, ranging from low relief erosional and depositional plains, to steep hills, ridges and escarpments (Wilford & Thomas 2012). Topographic relief proves to be a strong influence on soil properties, with small regions demonstrating inverse landscapes (Jackson 1957). The dominant soils in the area tend to be yellow-grey-brown podzols on slopes, with laterised podzols present along rocky ridge tops and northward facing slopes (Blackburn 1958). The variability and complexity of lithologies present controls the chemistry and physical properties of the overlying soil profiles (Jackson 1957). The area exhibits a Mediterranean-type climate and receives an average annual rainfall of 550-650mm (ForestrySA 2006). Pine plantation and native forest are the dominant vegetation types. Three sites with contrasting terrains, which are typically observed in the area, are used for the study. The location of the study sites within the Mount Crawford area are shown in Figure 1. A brief description of the traverse at each study site is given.

2.3.1 SITE 1: ROCKY PADDOCK

The first site, Rocky Paddock, is located within a sheep grazing field in the northwest corner of Figure 1 (centred on 311100mE; 6155950mN, WGS 84, zone 54S). The length of the traverse at this site is 240 m. Rocky Paddock shows the lowest topographic relief of the three sites. The topographic elevation profile of the traverse is presented in Figure 2. The traverse begins relatively flat in the northeast, with a slight decline heading southwest into a central saddle. Continuing along the transect, an incline that increases in slope towards the northeast is encountered. Nearby rock outcrops indicate

gneiss/migmatite bedrock at the start of the traverse, and a lithology change to schistose rocks near the central saddle.

2.3.2 SITE 2: CHALKIES LINE

The second site, Chalkies Line, site is located approximately 2.5 km south of Site 1 in the southern section of Figure 1 (centred on 313100mE; 6153450mN, WGS 84, zone 54S). The length of the traverse at this site is 480 m. It is located partially within native vegetation forest and partially alongside a pine plantation forest. A compacted gravel road splits the two vegetation types. The topographic elevation profile of the traverse is presented in Figure 3. The traverse begins on a hill crest, moving into a steep decline through native vegetation until encountering the gravel road. A ridge marks the start of

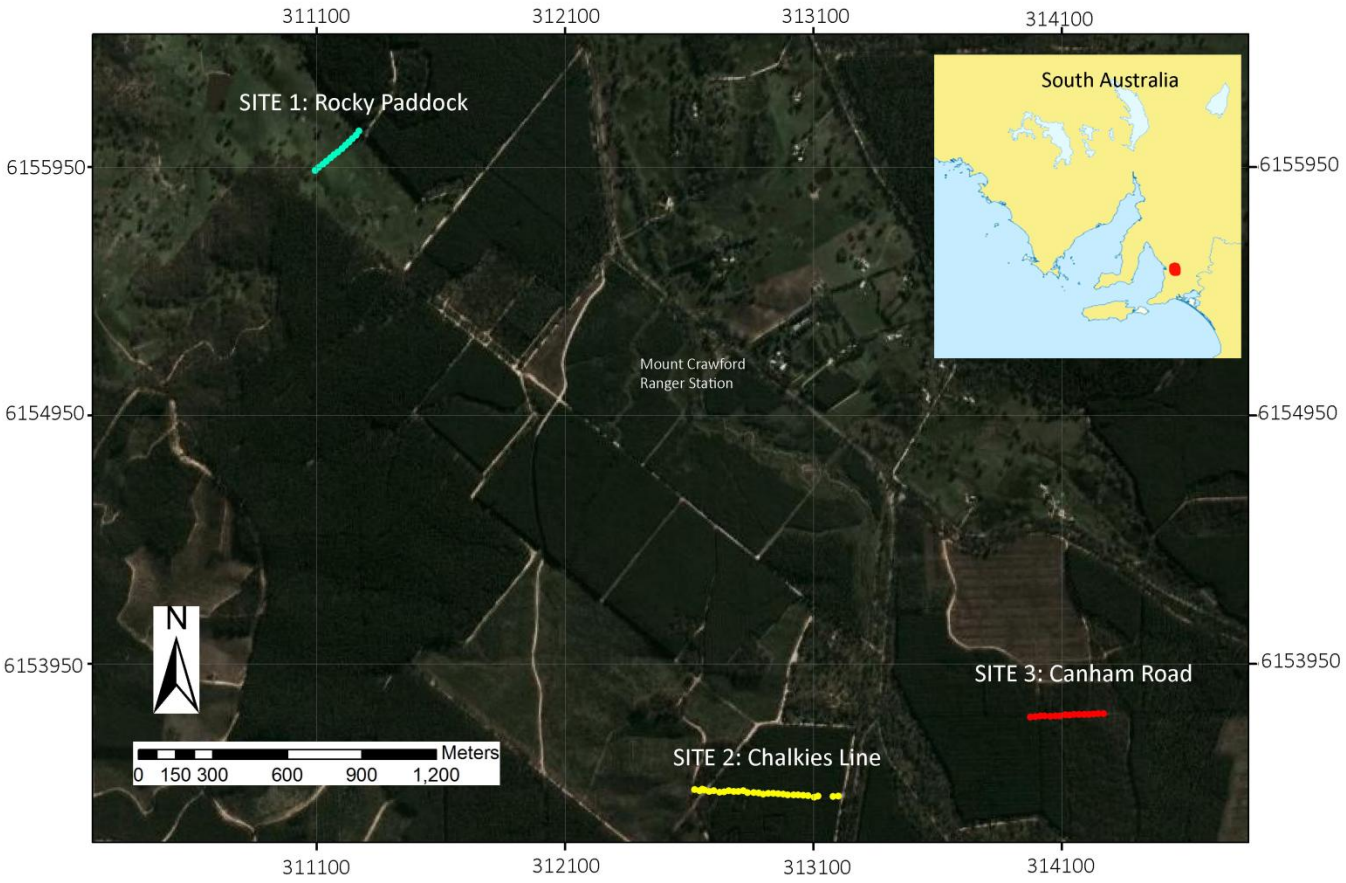

Figure 1: Locality map of the three survey lines within the Mount Crawford Forestry Reserve. The northern-most blue line indicates Site 1 (Rocky Paddock), the yellow line to the south indicates Site 2 (Chalkies Line), and the red line to the east indicates Site 3 (Canham Road). All co-ordinates were collected at drill locations, and are projected in WGS 84 (zone54s). Inset is a locality map of the region being investigated for this study (not to scale).

plantation forest, with a steep incline of the western ridge face. The remainder of the transect is relatively uniform, with a shallow decline heading eastward. The surface sediments appear to be rich in talc. Large scale quartzite and pegmatite outcrops were observed on the central ridge.

2.3.3 SITE 3: CANHAM ROAD

The third survey line is located approximately 1 km east of Site 2 (centred on 314100mE; 6155800mN, WGS 84, zone 54S). The length of the traverse at this site is 300 m, occurring wholly within native vegetation forest. The topographic elevation profile of the traverse is presented in Figure 4.The traverse begins atop a ridge with ferruginised soils. Moving westward, the traverse descends steeply for a distance of 50 m. Here it flattens temporarily, before continuing as a steep descent. The traverse ends in a shallow saddle which rises into a small ridge. An abundance of loose quartzite and ferruginised rocks are observed throughout the site, though never as an outcrop.

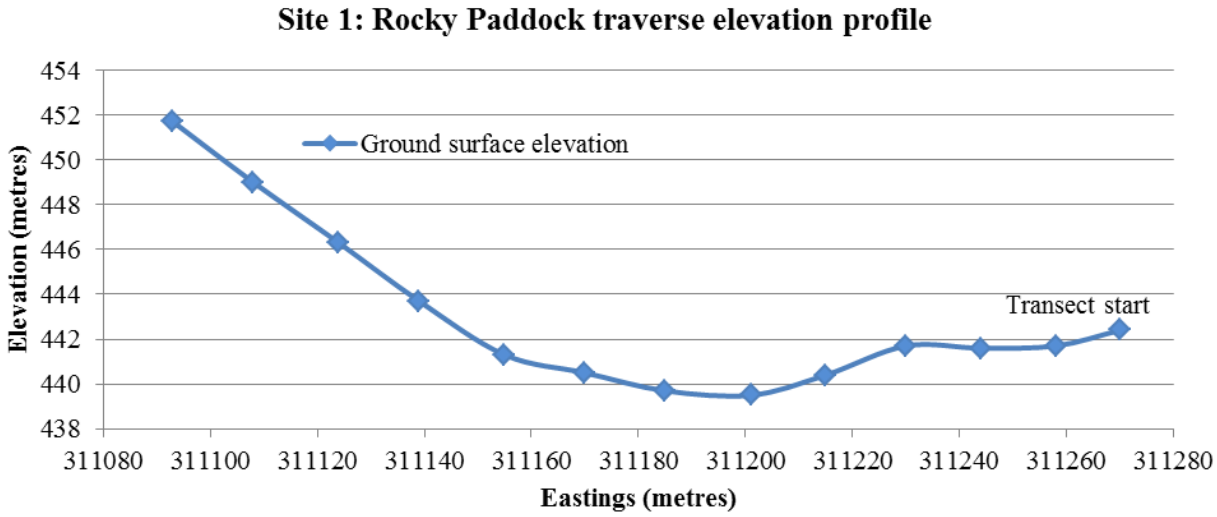

Figure 2: Topographic cross-section of the traverse at Site 1 (Rocky Paddock). Values were obtained using a differential GPS with 0.1 metre horizontal accuracy.

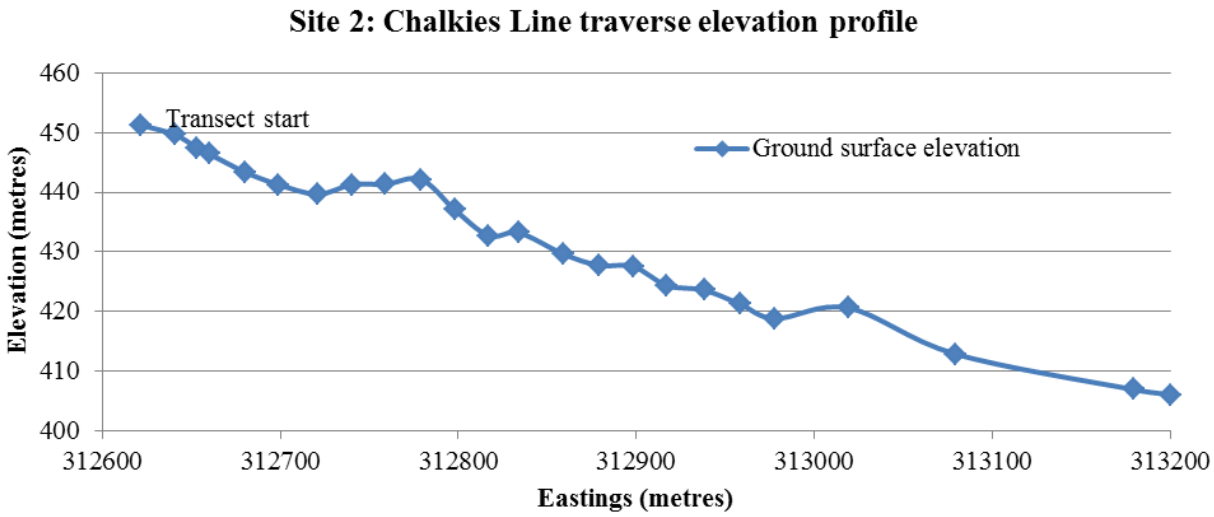

Figure 3: Topographic cross-section of the traverse at Site 2 (Chalkies Line). Readings were obtained using a differential GPS with 0.1 metre horizontal accuracy.

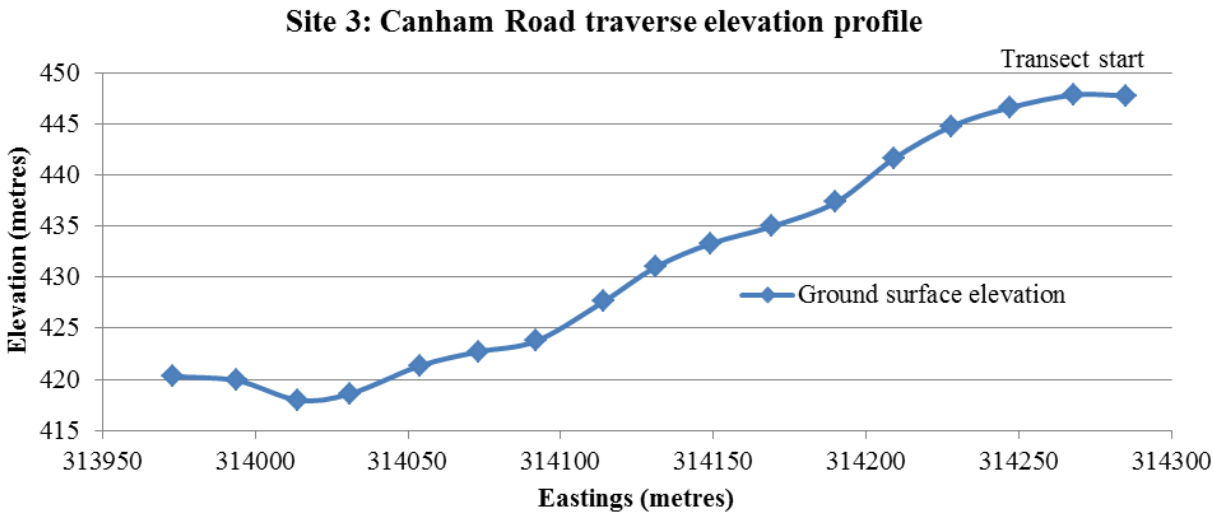

Figure 4: Topographic cross-section of the traverse at Site 3 (Canham Road). Readings were obtained using a differential GPS with 0.1 metre horizontal accuracy.

3. EQUIPMENT THEORY

3.1 Ground-penetrating radar

GPR readings are based upon the transmission and reflection of electromagnetic waves within a material under investigation (Chanzy *et al.* 1996). Under favourable conditions, the electromagnetic waves behave identically to acoustic waves (Cai & McMechan 1995). The system generates an electromagnetic wave train (signal) through a transmitter antenna (Reynolds 1997). Generated frequencies lie within the radio wave spectrum, between 10 MHz and 1000 MHz (Carcione 1996). The waves propagate in a 90^{o} cone beam along raypaths defined by Snell's law (Cai & McMechan 1995, Reynolds 1997). Waves interact with the subsurface, with contrasts in the dielectric properties at interfaces causing part of the incident signal to be reflected (Davis & Annan 1989). Du and Rummel (1994) explain the multiple sources of propagating waves that the receiver may detect (see Figure 5).

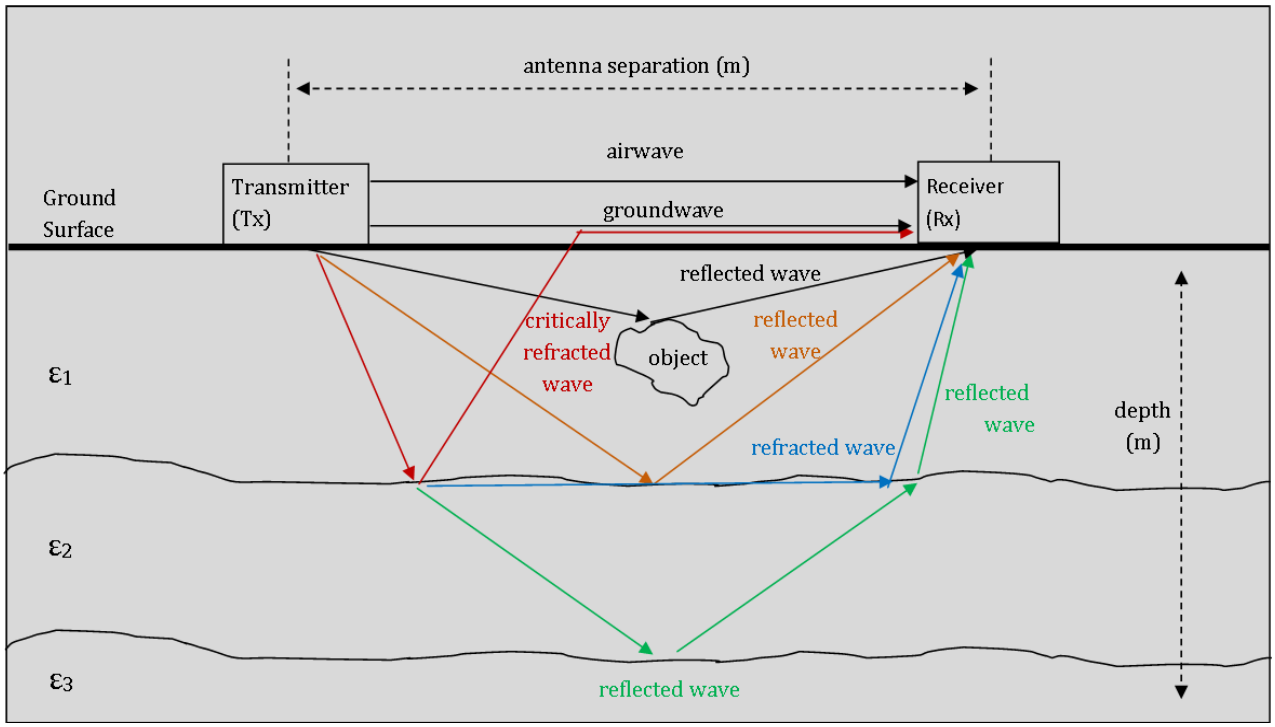

Figure 5: Schematic diagram of potential radio wave propagation paths generated by a GPR transmitter. Note that the airwave is received before any other transmitted wave. Modified after Du and Rummel (1994)

The propagation of electromagnetic waves from a GPR transmitter is described by Maxwell's equations (Reynolds 1997, Annan 2005). The speed of waves (***v***) in a material is given Reynolds (1997) as:

$$\boldsymbol{v} = c/\sqrt{\left\{\left(\frac{\varepsilon_r \mu_r}{2}\right)[(1+P^2)+1]\right\}}, \quad (1)$$

where c is the speed of light in free space (0.3 m/ns), ε_r is relative dielectric constant, and μ_r is the relative magnetic permeability of the material ($\mu_r = 1$ in the case of non-magnetic materials). The value P is the "loss tangent" of a material, described by Annan (2005) as:

$$P = \tan\theta = \frac{\sigma}{\varepsilon\omega}, \quad (2)$$

where σ is the bulk conductivity in S/m, and $\omega = 2\pi f$ where f is the angular frequency. Reynolds (1997) defines the dielectric permittivity $\varepsilon = \varepsilon_r \varepsilon_0$ where ε_r is the dielectric constant and ε_0 is the permittivity of free space (8.854 x 10^{-12} F/m). In low-loss geological media, P is ≈ 0 (Annan 2005). Hatch *et al.* (2013) refine the definition of low-loss geological media to have P = ≤0.69. In these conditions displacement currents remain the primary method of energy propagation, thus providing a suitable setting for GPR wave transmission (Hatch *et al.* 2013). Where P= ≥0.69, conduction currents begin affecting energy propagation. These conditions are no longer considered low-loss, and attenuation by conductivity becomes significant (Hatch *et al.* 2013). In low-loss material, where P = ≤0.69, Davis and Annan (1989) give the condensed solution for radar signal velocity as:

$$\boldsymbol{v} = \frac{c}{\sqrt{\varepsilon_r}} \quad (3)$$

The contrast in ε_r between contacting subsurface layers dictates the reflection amplitude of the transmitted incident signal. Reynolds (1997) shows that with greater ε_r contrasts, larger reflections amplitudes are generated. Assuming no signal is lost loss from factors such as energy decay and attenuation, Annan (2005) gives the amplitude reflection coefficient (*R*) as:

$$R = \frac{\sqrt{\varepsilon_1} - \sqrt{\varepsilon_2}}{\sqrt{\varepsilon_1} + \sqrt{\varepsilon_2}}, \tag{4}$$

where ε_1 and ε_2 represent the respective dielectric constants between two contacting subsurface layers (see Figure 5). Reynolds (1997) notes that in all circumstances, the amplitude range of *R* is always within a value of ± 1. Various factors reduce wave energy available to be reflected at deeper events as the signal propagates through the subsurface (Olhoeft 1986). Wave energy is reduced per unit area at a rate of $1/r^2$ where r is the distance travelled as a result of the incident beam spreading, and energy lost as heat (Annan 2005). Attenuation (dB/m) of signal is a significant factor influencing signal penetration depths (Olhoeft 1986). Reynolds (1997) gives the attenuation factor (α) of GPR signal as:

$$\alpha = \omega\left\{\left(\frac{\mu\varepsilon}{2}\right)\left[\left(1 + \frac{\sigma^2}{\omega^2\varepsilon^2}\right)^{1/2} - 1\right]\right\}^{1/2}, \tag{5}$$

where σ is the bulk conductivity (S/m), and μ is the magnetic permeability ($4\pi \times 10^{-7}$ H/m). This shows signal attenuation to be product of the dielectric, magnetic and electric properties of the material hosting the signal. Annan (2005) describes attenuation to be proportional to the incident wave frequency. In low-loss materials, Annan (2005) collapses the attenuation equation, giving the solution:

$$\alpha = \frac{\mu\sigma\boldsymbol{v}}{\sqrt{2}} \quad (6)$$

The attenuation factor of the material under investigation directly influences the maximum depth of signal penetration (Olhoeft 1986). The depth at which the incident radar signal has decreased in amplitude to 37% of initial value is known as the skin depth (δ). Reynolds (1997) describes skin depth to be inversely proportional to α, given as:

$$\delta = 1/\alpha \quad (7)$$

Reynolds (1997) suggests that the simplified skin depth equation is valid only when P = ≤1. Reynolds (1997) gives the solution for instances when P = ≥1 as:

$$\delta = \left(5.31\sqrt{\varepsilon_r}\right)/\sigma \quad (8)$$

This suggests that penetration depth in materials with P = ≥1 is proportional to ε_r and σ. Signal attenuation and skin depth are not the only variables that affect penetration depth (Olhoeft 1986). Radar signal can be scattered by subsurface inhomogeneity when the incident signal wavelength (λ) is 3-10 times smaller than the reflecting object (Doolittle & Collins 1995). Signal scatter appears as attenuation on the GPR radargram (Reynolds 1997). Du and Rummel (1994) give the signal wavelength as:

$$\lambda = c/(f\sqrt{\varepsilon_r}) \quad (9)$$

Higher frequency antennae have smaller wavelengths, thus are more susceptible to signal scatter than lower frequency antennae (Doolittle & Collins 1995). The use of different frequencies determines the vertical resolution (z) of a signal (Annan 2005). The vertical resolution of a GPR system is the smallest difference in time (ns) between

two objects that the system can detect before resolving both reflections as a singular object (Reynolds 1997). The maximum theoretical vertical resolution of the GPR signal is ¼ of the incident raypaths pulse wavelength, given by Reynolds (1997) as:

$$z = \boldsymbol{v}/(4f) \tag{10}$$

The solution determines that to achieve higher levels of vertical resolution, it is necessary to use higher frequency antenna (Annan 2005). Horizontal resolution is described as the equivalent of vertical resolution, but on the x-axis of the radargram (Charlton 2008). This value is independent of vertical resolution. Horizontal resolution is inversely proportional to the square root of attenuation, (Reynolds 1997). Thus, higher horizontal resolution is observed in low loss material. As a result, target depth and desired resolution must be considered when selecting antennae frequencies for a GPR survey. Reynolds (1997) and Annan (2005) further explain GPR theory beyond the scope of this paper.

3.2 Electrical resistivity

Electrical resistivity surveys are used in soil science to determine the distribution of resistivity contrasts within a soil volume (Banton *et al.* 1997). Low frequency alternating current is generated by an external power source and delivered to the soil via emplaced electrodes (Zhe *et al.* 2007). The flow line distributions of the induced current depend on the medium being investigated, with higher concentrations occurring in conductive areas (Zonge *et al.* 2005). Samouelian *et al.* (2004) identified the nature of soil constituents (particle size and mineralogy), porosity (pore size, distribution and connectivity), water saturation, fluid ionic concentration and temperature to be the main characteristics affecting a soils resistivity. Zonge *et al.* (2005) suggests the apparent

resistivity ($\rho_{a)}$ of a material to be proportional to the current induced (I), voltage ($\Delta\Phi$) and geometric factor of the electrodes (G), giving the solution:

$$\rho_a = G\frac{\Delta\Phi}{I} \tag{11}$$

Reynolds (1997) and Zonge *et al.* (2005) further explain electrical resistivity theory beyond the scope of this paper.

3.3 Electromagnetics

EM systems generate electromagnetic waves by passing an alternating current through a transmitter loop (Reynolds 1997). This generates a primary magnetic field that propagates above and below the ground surface (Telford *et al.* 1990). The magnetic component of the primary field induces eddy currents in any subsurface conductors (Reynolds 1997). The eddy currents generate a secondary electromagnetic field which is detected by a receiver coil placed at a predetermined distance and orientation to the transmitter coil (Fitterman & Labson 2005). The receiver simultaneously detects the primary and secondary fields, giving an output of the combined magnetic field values that differ in phase and amplitude to the original primary wave (Reynolds 1997). McNiell (1980) identifies the quadrate phase component of the detected electromagnetic fields to be linearly proportional to ground conductivity, giving the solution as:

$$\sigma_a = \frac{4}{\mu_0 \omega s^2}\left(\frac{H_s}{H_p}\right), \tag{12}$$

where μ_0 is the permittivity of free space, H_p is the detected primary magnetic field, and H_s is the detected secondary magnetic field. The difference in phase and amplitude between the primary and secondary magnetic fields provides information on the size, geometry and electrical properties of any detected subsurface conductors (Reynolds

1997). This solution only applies to systems operating at low induction numbers (McNiell 1980). Fitterman and Labson (2005) further explain EM induction theory beyond the scope of this paper.

4. METHODS

4.1 Ground-penetrating radar

A MALÅ Geoscience X3M control unit was for GPR surveying at each site. In order to identify the optimal frequency to discern depth to bedrock, 100-MHz, 250-MHz, 500 MHz and 800 MHz fixed-separation shielded antennae were used. Traverses were made at each site parallel to marked drilling locations. Operational parameters, sampling rates and theoretical maximum signal penetration depths are presented in Table 1. Signal penetration depths are approximate and are provided by MALÅ Geoscience (MALA Geoscience 2013). Differential GPS readings were obtained concurrently with GPR data. Processing was completed using ReflexW 2D GPR processing software. Results were subject to the following processing steps; Subtract mean (DeWow), background noise removal, static correction of the first arrival, F-K migration, signal enveloping and running average smoothing filter. The plots were migrated using a velocity function determined by the shape and size of visible reflections (v = 0.14 m/ns). Bedrock depth predictions were made using automatic phase-follower picking in ReflexW, using an amplitude cut-off value of 0.25. Comparative data analysis of GPR estimates were completed using Excel data analysis software. Appendix A contains a detailed explanation of field methodology, survey parameters and processing steps.

Table 1: Operational parameters of all GPR antennae used at each site. Note the theoretical maximum depths of signal penetration suggested for each antennae. The interval represents the volume of data traces collected over a given distance (250, 500, 800 MHz), or time (100 MHz).

Antenna	100 MHz	250 MHz	500 MHz	800 MHz
Time Window	198.6 ns	140.0 ns	78.8 ns	39.6 ns
Theoretical Max Depth	10.18 m	7.18 m	4.03 m	2.05 m
Point (m) or Time (s) Interval	0.25 s	0.05 m	0.04 m	0.019 m
Samples Per Interval	344	536	624	512
Sampling Frequency	1581.25 MHz	3614.29 MHz	7535.71 MHz	12173.08MHz
Antennae fixed offset	0.5 m	0.36 m	0.18 m	0.14 m

4.2 Electrical resistivity

A ZZ Resistivity Imaging FlashRES-64 system was used for electrical resistivity surveying at each site. Each spread of the resistivity instrumentation consisted of 64 electrodes at 1.5 m spacing. Direct current voltage outputs per electrode were 120 V at 250 W (240 V per electrode pair). Differential GPS locations were obtained at pre-determined electrode spacings. Proprietary ZZ Resistivity Imaging software was used to invert the data. Zhe *et al.* (2007) provides background on the acquisition system and basics of operation. Zhou and Greenhalgh (1999) explain the 2.5D inversion process. Plots of inversion outputs were constructed using Surfer gridding software. Data inversion, processing and gridding were completed externally (T. Fotheringham pers. comm. 2013). Appendix A contains full descriptions of equipment set-up, parameters, data inversion and processing.

4.3 Electromagnetics

A Geonics DualEM-421s frequency-domain system was used for EM surveying at each site. The DualEM-421s consists of 3 pairs of horizontal co-planar (HCP) and perpendicular (PRP) orientated receiver arrays (Geonics Limited 2013)A singular transmitter is shared by all arrays, operating at a frequency of 9 kHz. The orientation and depths of investigation for each array is detailed in Table 2.

Table 2: Receiver array orientation and depths of investigation for the DualEM-421 instrument. Data for all receivers is gather simultaneously.

Receiver orientation	HCP	HCP	HCP	PRP	PRP	PRP
Distance from receiver	1	2	4	1.1	2.1	4.1
Depth of measurements	0-1.5 m	0-3.0 m	0-6.0 m	0-0.5	0-1.0	0-2.0

The DualEM survey involved carrying the instrument along each traverse at a height of 0.30 m, using drill hole locations and a differential GPS to provide geo-referencing. DualEM data inversion was completed externally using EM4Soil processing software (J. Triantafilis pers. comm. 2013). Monteiro Santos *et al.* (2009) and Triantafilis *et al.* (2013) describe algorithms and software used for data inversion. The Krieging gridding method was used in Surfer gridding software to present the inverted data (T. Fotheringham pers. comm. 2013). Detailed field methods and steps of data processing are presented in Appendix A.

4.4 Drilling and soil analysis

Drilling was conducted using a Geodrill rig-mounted 60 mm push-tube percussion drill, with a maximum capable depth of 9 m. All drill holes terminated at drill refusal which, for the purpose of the project, was assumed to represent first contact with the R horizon (moderately weathered bedrock). Rocky Paddock was drilled from northeast to southwest (n =13), Chalkies Line from west to east (n = 24) and Canham Road from west to east (n = 17). Canham Road was drilled in the opposite traversal direction to the geophysical surveys. Drill hole locations (DH) were designated for each hole based upon the order of drilling. Coordinates obtained using a differential GPS at each drill location are available in Appendix B. Holes were drilled along each traverse at nominal 20 m intervals. Samples were obtained and logged at 0.30 m intervals; up to a depth of 1.50 m. Samples from depths greater than 1.5 m were obtained in 0.5 m increments. Moisture content and EC 1:5 analyses were conducted for each gathered soil sample. Detailed methods and procedures for these techniques are presented in Appendix A.

5. OBSERVATIONS AND RESULTS

Results are organised into sections based upon respective physiographic regions. Three sets of results presented for each site. The first set of results present a linear graph of the surface elevation of each traverse, measured using GPS, plotted against drill refusal depths. The site topography profiles have elevation (m) plotted on the vertical axis with location determined by GPS coordinates (eastings) on the horizontal axis. The second set of results shows a visual comparison of processed GPR antennae plots for all four antenna frequencies. Each GPR plot has the horizontal axis as distance (m) and the vertical axis representing both time (ns) and depth (m). Depths were calculated using a velocity of 0.14m/ns, as determined during data processing. The third set of results presents the inverted electrical resistivity and DualEM-421s data, with distance (m) along the horizontal axis, and depth (m) along the vertical axis. All EM and electrical resistivity data are converted to resistivity values (ohm-m). The GPR antenna that provides the best balance between resolution and penetration depth for each site is compared to these plots, using GPS coordinates to align each of the data sets. Drill hole locations and refusal depths are marked on each of the plots. Bedrock depth estimates are presented for the selected GPR antenna. For comparative reasons, the data for each technique has been constrained to where data is available for all techniques. Paired *t* means tests (α=0.05) are used to test the correlation of bedrock depth estimates from the GPR antenna frequency that best displayed signal reflections and drill refusal depths at each site. This presents a mathematically based assessment of bedrock depth correlations. Secondary paired *t* test results are also presented for bedrock depth estimates in areas showing resistive subsurface units. All soil analysis data and profile logs are compiled in Appendix B.

5.1 Site 1: Rocky Paddock

Figure 6 shows the depth of drill refusal along the traverse at Site 1, relative to surface elevation. The depth of refusal varies from 1.35 m at DH 1.04, to a maximum of 4.7 m at DH 1.05. Across the traverse the refusal depths tend to remain relatively constant, with a mean depth of 2.09 m. Gneissic and schistose outcrops were obsered in close proximity to the survey line.

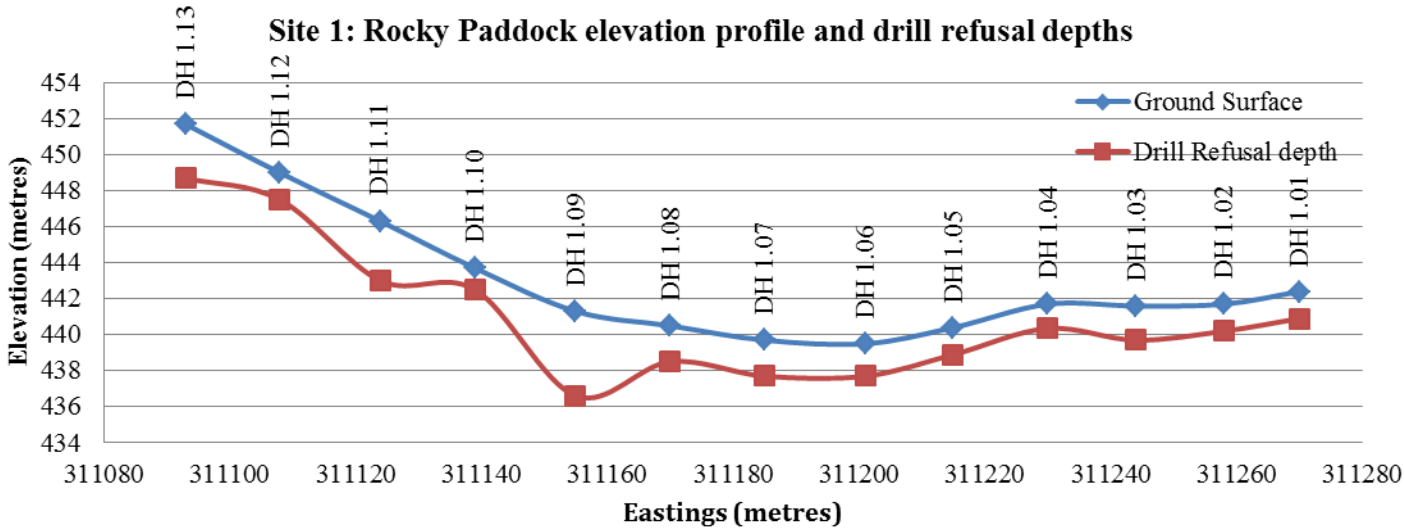

Figure 6: Cross-section of the Site 1 traverse. Drill hole locations and depths are marked relative to regional topography.

Figure 7 presents the plots of processed ground-penetrating radar data from the lowest antennae frequency, 100 MHz (Figure 4a), to the highest, 800 MHz (Figure 4d), across traverse at Site 1. Moving from left to right, signal penetration depth for all antennae appears to be greatest at the start of the transect. A small scale attenuation feature is seen on the 250 MHz and 800 MHz antennae at 20-40 m. Signal penetration depth remains constant throughout the profile, only marginally decreasing towards the end of the survey line. The raw data in Appendix C show negligible reflection hyperbola for all four antennae frequencies.

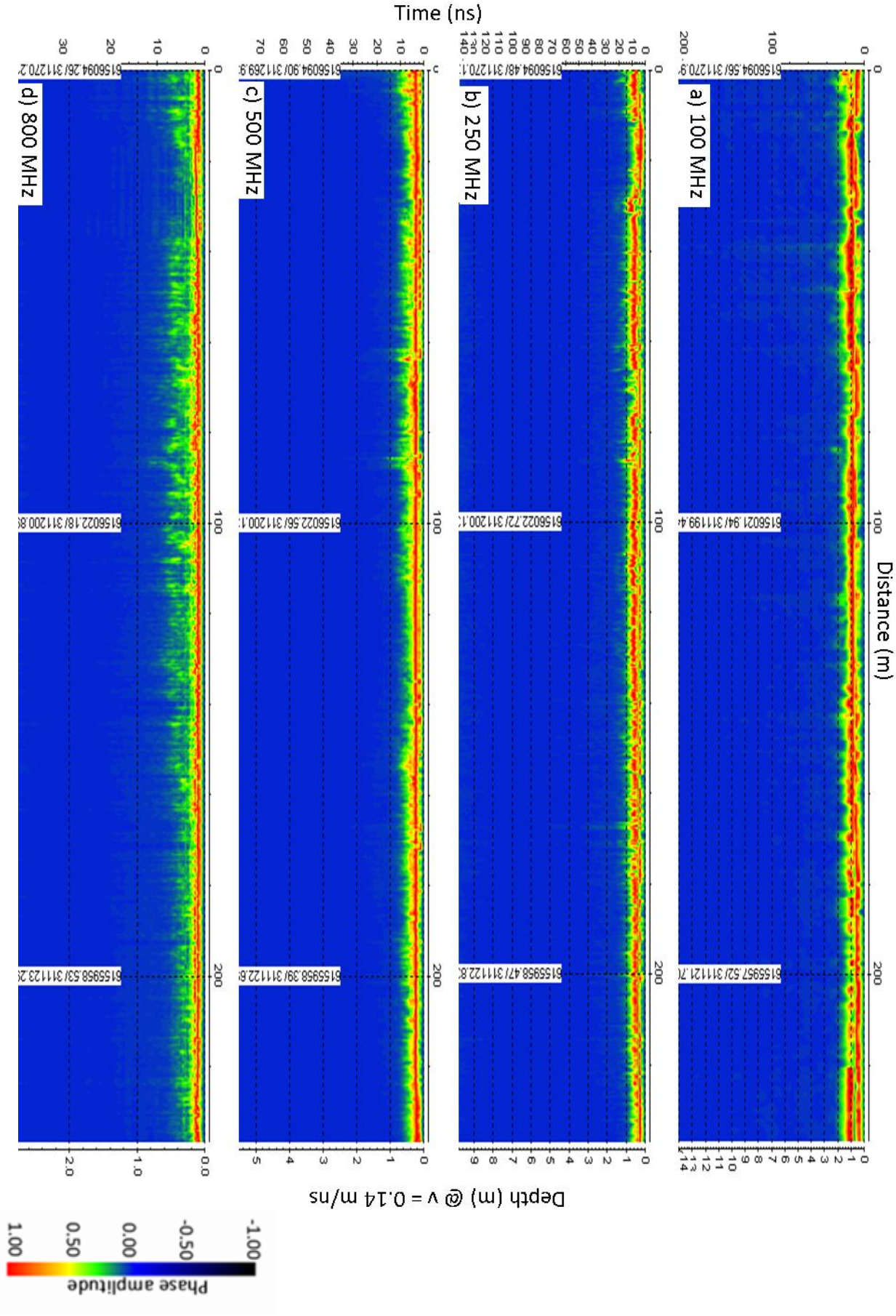

Figure 7: Comparative plot of processed ground-penetrating radar data for Site 1 (Rocky Paddock), showing; a) 100 MHz, b) 250 MHz, c) 500 MHz and d) 800 MHz antenna results. Note that y-axis depth is a function of signal velocity (m/ns) and time (ns). The time windows for each antennae (presented in table 1) dictate the maximum depth of which data can be presented.

The GPR results for all antennae from Site 1 do not reach the expected signal penetration depths. The 800 MHz signal reaches penetration depths ranging from 0.46 to 0.81 m, which are only marginally exceeded by the 250 MHz and 500 MHz signal. The 100 MHz signal fares slightly better, reaching an approximate depth of 2 m. The 800 MHz antenna gives the greatest vertical resolution of all the plots while still identifying all features recognised in the other antennae. The depth of penetration and resolution of the 800 MHz antenna provided an acceptable representation of GPR signal profiles to be used in depth estimate comparisons with data from the other techniques. Figure 8 presents a comparison plot of the 800 MHz GPR, electrical resistivity and DualEM results, with added GPR bedrock depth estimates and drill refusal depths.

The electrical resistivity (Figure 8a) and DualEM (Figure 8b) results show a largely resistive subsurface starting at DH 1.01, with a change to a more conductive subsurface occurring at the mid-point of the survey line, at DH 1.08. The resistive features range in resistivity value from 500-1000 ohm-m. Conductive subsurface resistivity values average to approximately 100 ohm-m, with minor conductors present with values of 1 ohm-m. The GPR signal shows little to no variation in response when transitioning between the two ground types, with the signal not penetrating to depths great enough to be affected by the apparent lithology change. Gneissic outcrop is present within 50 m of the resistive sections, perpendicular to the survey line. Drill refusal depths appear to be shallower and relatively uniform in these resistive areas, compared to the conductive areas where schistose outcrop is observed.

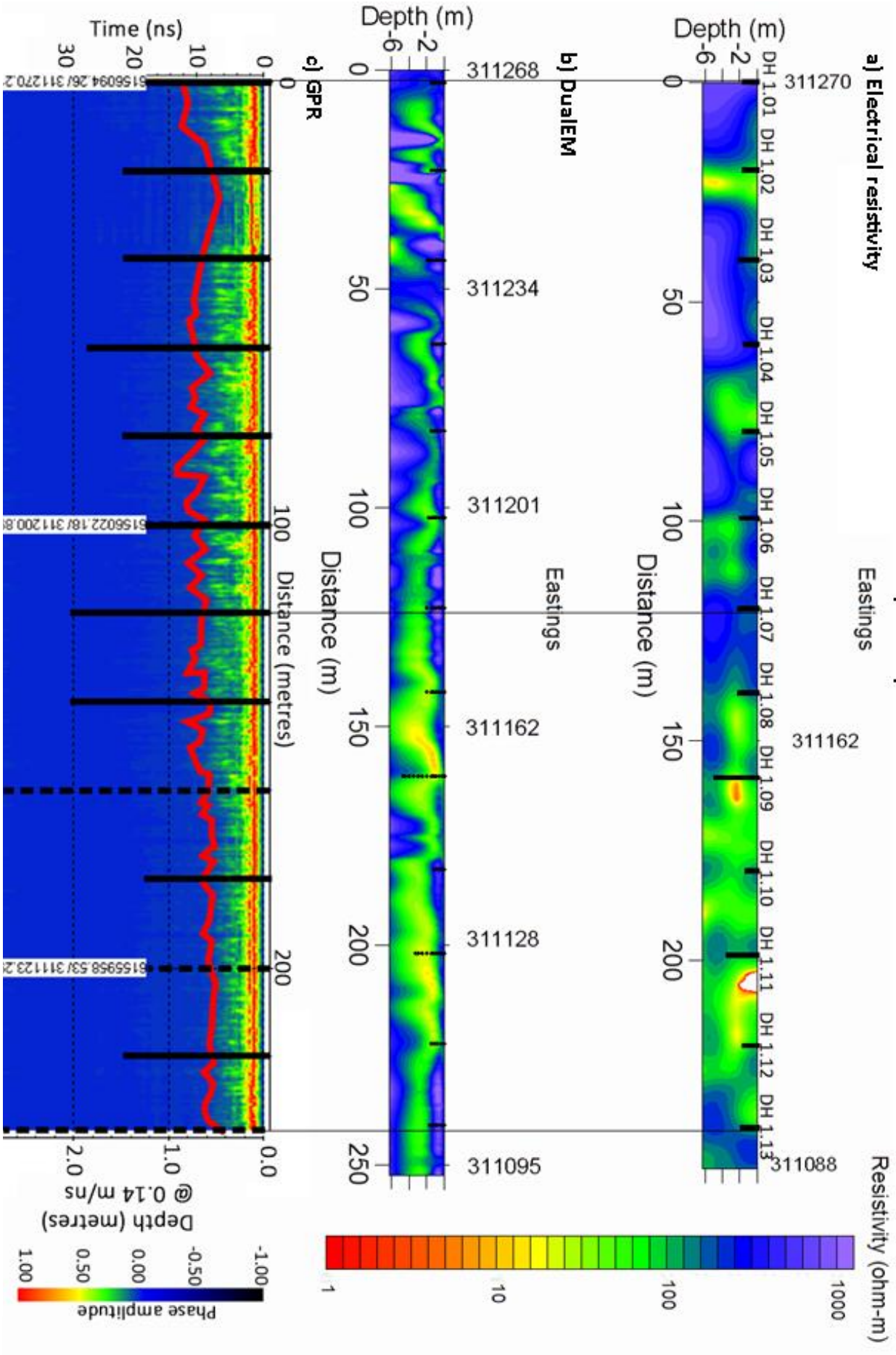

Figure 8: Comparison plot for Site 1 showing: a) electrical resistivity, b) DualEM and c) GPR results. Drill locations and depths are marked on all plots by black lines, with dashed black lines indicating drill depths that exceed the maximum depth of the plot. Estimated GPR bedrock depth is marked on the GPR radargram, represented by a horizontal red line. Plots are aligned by drill hole coordinates. Note that the EM and resistivity results are to a depth of 6 m, compared to GPR radargram depth of ~2.6 metres.

The 800 MHz GPR antenna bedrock depth estimates at each of the drill locations are compared with the drill refusal depths at the same localities. A paired *t*-means test was conducted to test the correlation between the two methods, the results of which are presented in Table 3. The Pearson correlation value of -0.28 indicates no correlation between the GPR estimates and drill refusal depths for the whole line (n = 13). Table 4 presents a second paired *t*-means test using GPR estimations and drill refusal depths located within resistive areas (n = 4), giving a Pearson correlation of -0.95. The Pearson correlation values suggest GPR bedrock depth estimates and drill refusal depths share no correlation, regardless of subsurface conductivity conditions.

Table 3: Paired *t*-test to establish mean value and Pearson correlation between drill refusal depth and GPR bedrock depth estimates at Site 1.

t-Test: Paired Two Sample for Means		All Drill Holes
	Drill	*GPR*
Mean	2.096153846	0.609230769
Variance	0.997692308	0.012041026
Observations	13	13
Pearson Correlation	-0.286284639	

Table 4: Paired *t*-test to establish mean value and Pearson correlation between drill refusal depth and GPR bedrock depth estimates at Site 1, using only data from locations in areas with large scale resistive subsurface.

t-Test: Paired Two Sample for Means		Resistive Areas
	Drill	*GPR*
Mean	1.6875	0.69
Variance	0.097291667	0.0178
Observations	4	4
Pearson Correlation	-0.949181517	

5.2 Site 2: Chalkies Line

Figure 9 shows the depth of drill refusal along the transect from Site 2, relative to surface elevation. The depth of refusal varies significantly over the traverse, ranging from 0.60 m at DH 2.23, to a maximum of 7.30 m at DH 2.06. The drill tends to reach greater depths in areas with flat topography, at the base of shallow inclines. An exception to this is DH 2.10, which reaches a refusal depth of 5.20 m while being located on a topographic high. Mean drill depth at the site is measured to be 2.81 m. Field observations of nearby outcrop in the resistive areas found quartzite bedrock exposed in close proximity to the survey line, along with large scale pegmatites outcropping 50 m north of DH 2.08.

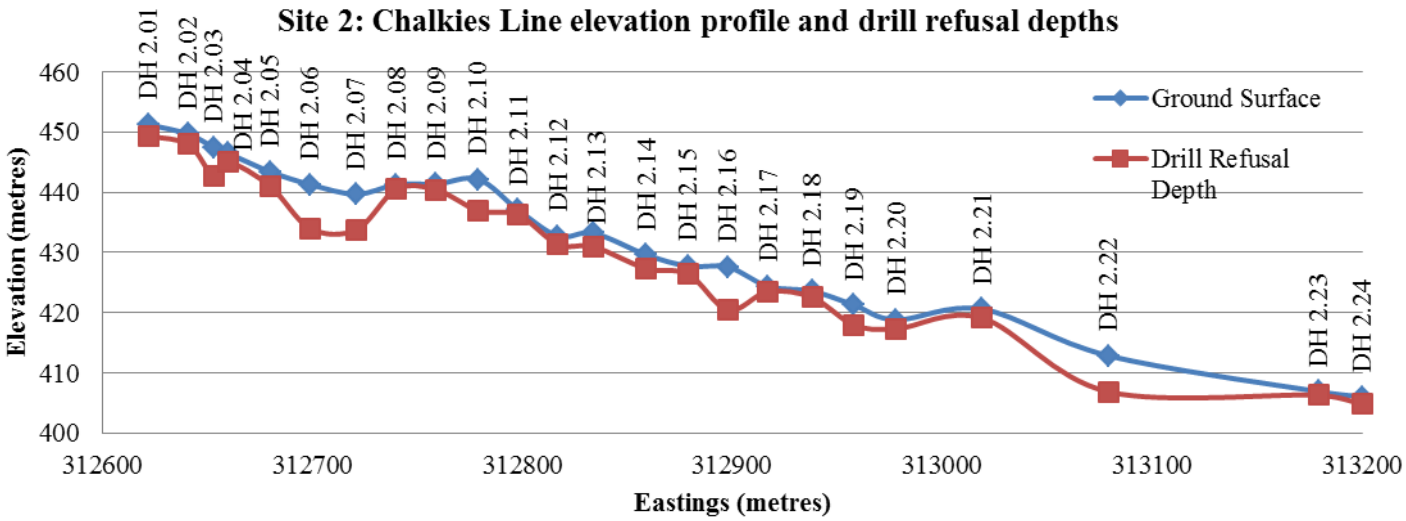

Figure 9: Cross-section of the Site 2 traverse. Drill hole locations and depths are marked relative to regional topography.

Figure 10 shows the plots of processed ground-penetrating radar data from the lowest antennae frequency, 100 MHz (Figure 10a), to the largest, 800 MHz (Figure 10d), across the Site 2 traverse. Moving from left to right, a small scale reflection is observed at 60 m in the 250 MHz, 500 MHz and 800 MHz antennae. All three of the higher frequency antennae detect a relatively high density of reflections from 120 to 200 m.

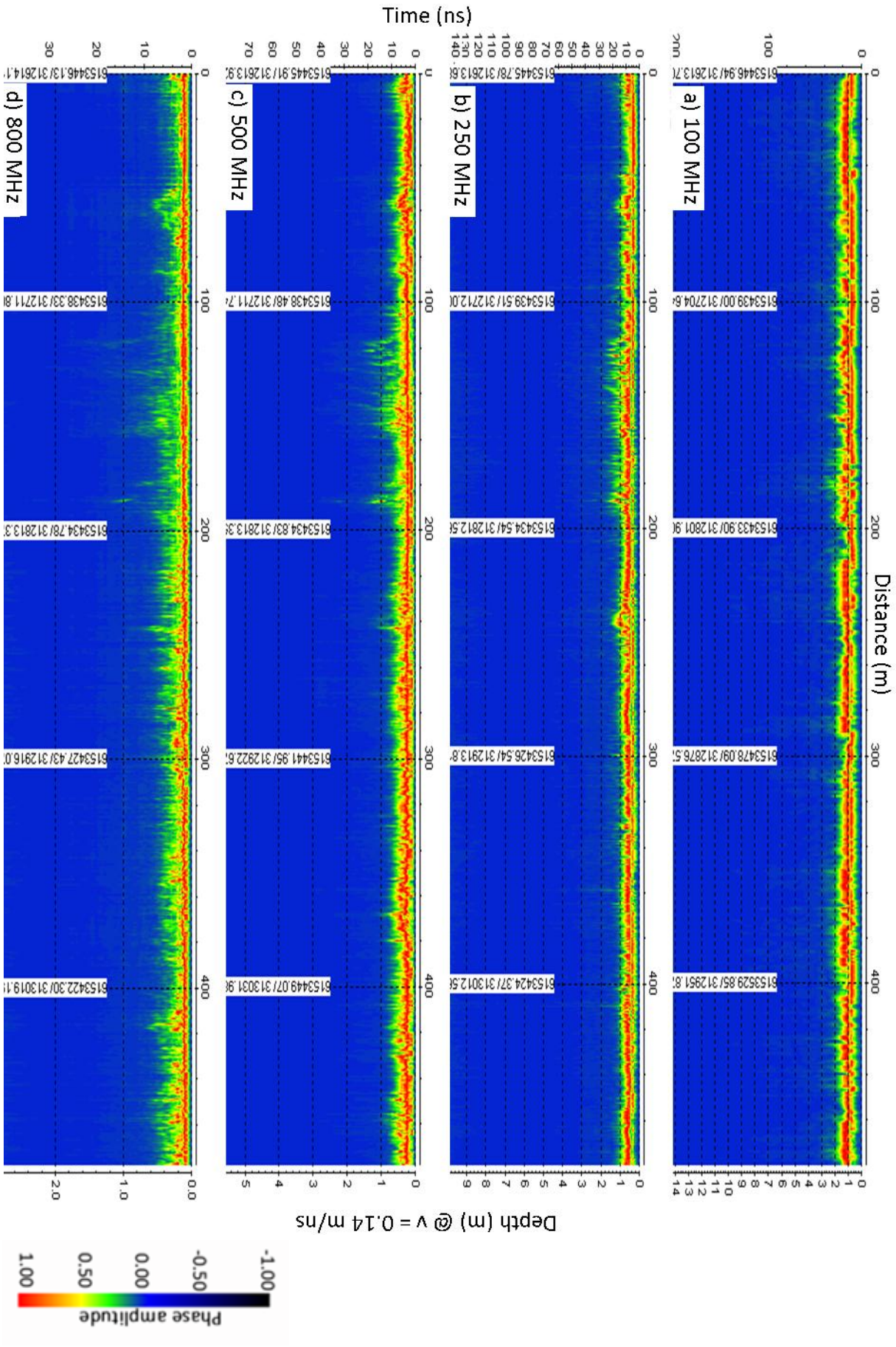

Figure 10: Comparative plot of processed ground-penetrating radar data for Site 2 (Chalkies Line), showing; a) 100 MHz, b) 250 MHz, c) 500 MHz and d) 800 MHz antenna results. Note that y-axis depth is a function of signal velocity (m/ns) and time (ns). The time windows for each antennae (presented in table 1) dictate the maximum depth of which data can be presented for each antennae.

The 100 MHz antenna does not identify either of these reflectors. A small reflector is recognised at approximately 180 m that is only detected by the 500 MHZ and 800 MHz antennae. A small scale attenuation feature is seen by the 250 MHz and 800 MHz antennae at 20-40 m. Signal penetration depth remains constant, only marginally decreasing towards the end of the transect. The GPR results for all antennae from Site 2 do not reach the expected penetration depths. The 800 MHz signal reaches penetration depths ranging from 0.48 to 1.03 m, which are only marginally exceeded by the 250 MHz and 500 MHz signals. The 100 MHz signal fares slightly better, reaching an approximate depth of 2 m. The 800 MHz antenna gives the greatest vertical resolution of all the plots while still identifying all features recognised in the other antennae. The depth of penetration and resolution of the 800 MHz antenna provided an acceptable representation of GPR signal profiles to be used in depth estimate comparisons with data from other techniques. Figure 11 shows a comparison plot of the 800 MHz GPR, electrical resistivity and DualEM results, with added GPR bedrock depth estimates and drill refusal depths.

The electrical resistivity (Figure 11a) and DualEM (Figure 11b) results show a general trend of conductive subsurface with a highly conductive lateral feature, reaching resistivity values as low as 0.063 ohm-m, dominating from 2 to 4 m depth. This conductive feature is present along most of the profile. A large scale highly resistive body is detected in the central section of the traverse, starting 10 m east of DH 2.07, and terminating 10 m west of DH 2.10. The lateral conductive feature does not occur within the resistive body. Minor, shallow resistive bodies occur to the west of the central resistive feature.

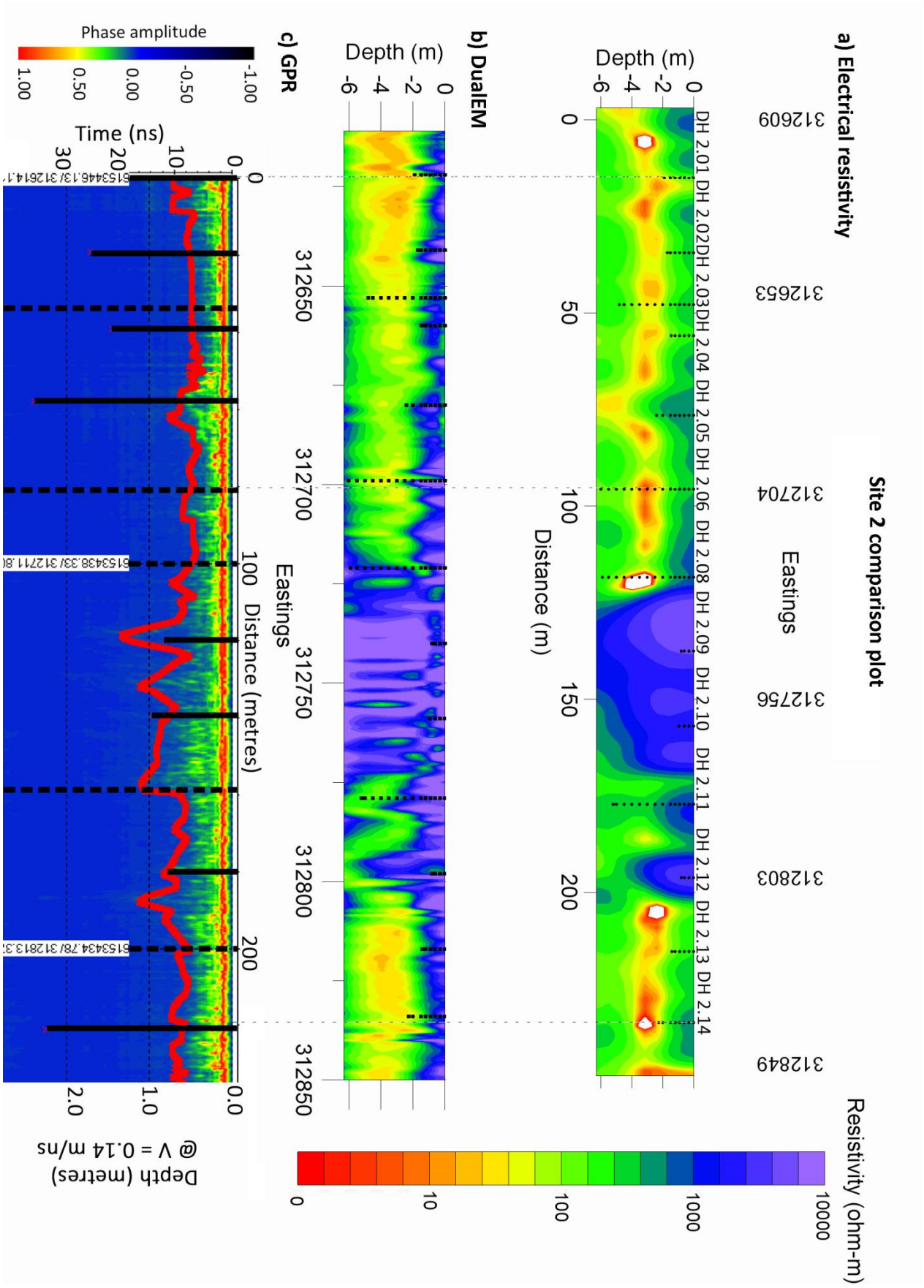

Figure 11: Comparison plot for Site 2, showing: a) electrical resistivity, b) DualEM and c) GPR results. Drill locations and depths are marked on all plots by black lines, with dashed black lines indicating drill depths that exceed the maximum depth of the plot. Estimated GPR bedrock depth is marked on the GPR radargram, represented by a horizontal red line. Plots are aligned by drill hole coordinates. Note that the EM and resistivity results are to a depth of 6 m, compared to GPR radargram depth of ~2.6 metres.

The resistive bodies have values ranging from 1000 – 10 000 ohm-m. DH 2.01- 2.05, DH 2.12 and DH 2.13 hit refusal at first contact with the conductive feature. The resistive areas correspond with areas of increased penetration depth in the processed GPR data, and hyperbola in the raw GPR data (see Appendix D). The GPR signal outside of the resistive sections show minor reflections, with extended sections showing zero reflections and complete signal attenuation. Shallow drill refusal corresponds with resistive subsurface at DH 2.08, DH 2.09 and DH 2.11.

The bedrock depth estimates provided by the 800 MHz GPR antenna at each of the drill locations were compared with the drill refusal depths at the same localities. A paired *t* means test was conducted to test the correlation between the two methods, the results of which are presented in Table 5. A second paired *t* means test was conducted using drill refusal and GPR bedrock depth estimate data collected at DH 2.08, DH 2.09, DH 2.10 and DH 2.11, which are all located within resistive bodies identified in Figures 11a and 11b. The results of the second paired *t* means test are presented in Table 6. In the resistive areas the Pearson correlation value is 0.97, showing a strong correlation between GPR depth estimates and drill refusal depths . These results use a small sample size (n = 4) due to the low drill count through the resistive bodies. The Pearson correlation value over the entire survey line (n = 22) is -0.17, showing no correlation between the GPR and drill refusal depths.

Table 5: Paired *t*-test to establish mean value and Pearson correlation between drill refusal depth and GPR bedrock depth estimates at Site 2.

t-Test: Paired Two Sample for Means		All Drill Holes
	Drill	*GPR*
Mean	2.811363636	0.638181818
Variance	4.729269481	0.021767965
Observations	22	22
Pearson Correlation	-0.177361429	

Table 6: Paired *t*-test to establish mean value and Pearson correlation between drill refusal depth and GPR bedrock depth estimates at Site 2, using only data from locations in areas with large scale resistive subsurface.

t-Test: Paired Two Sample for Means		Resistive Areas
	Drill	*GPR*
Mean	1.9375	0.88
Variance	4.735625	0.0108
Observations	4	4
Pearson Correlation	0.970585937	

5.3 Site 3: Canham Road

Figure 12 shows the depths of drill refusal along the transect from Site 3, relative to surface elevation. The depth of refusal varies from 0.40 m at DH 3.23 to a maximum of 6.80 m at DH 3.16, with a mean depth of 2.38 m. Refusal depths tend to increase at lower elevations, with the deepest refusal point (DH 2.16) located at a topographic low. Refusal depth is significantly shallower at topographic highs, where abundance of loose quartzite and iron stones are present, suggesting a change to the soil profile relative to topography.

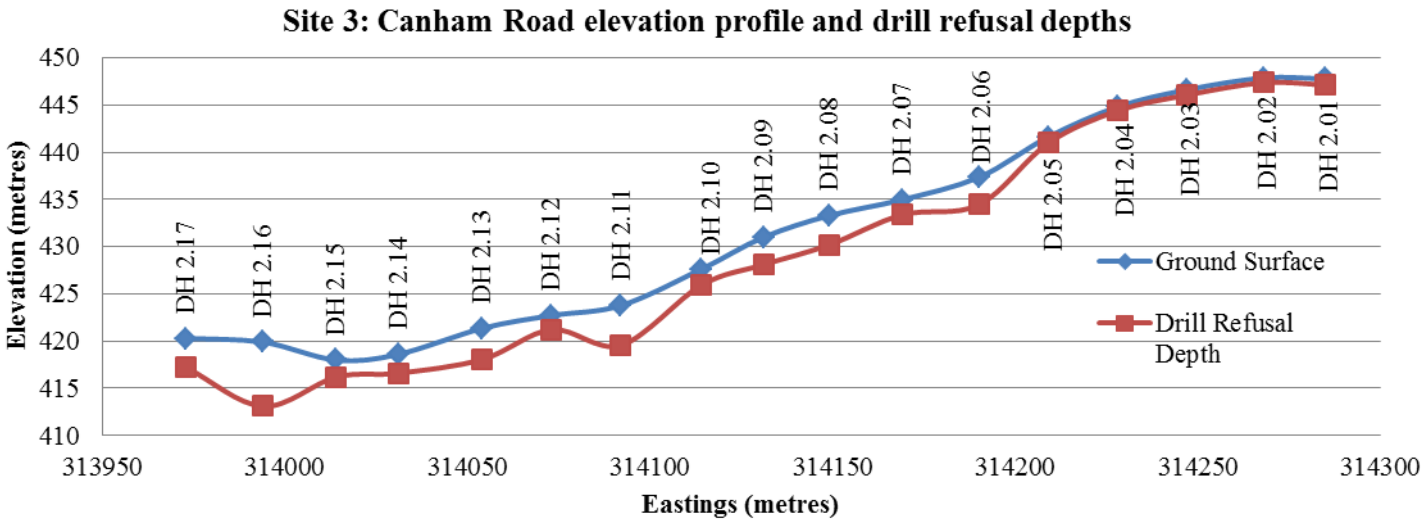

Figure 12: Cross-section of the Site 3 traverse. Drill hole locations and depths are marked relative to regional topography.

Figure 13 shows the plots of processed ground-penetrating radar data from the lowest antennae frequency, 100 MHz (Figure 13a), to the highest, 800 MHz (Figure 13d), across the traverse ate Site 3.

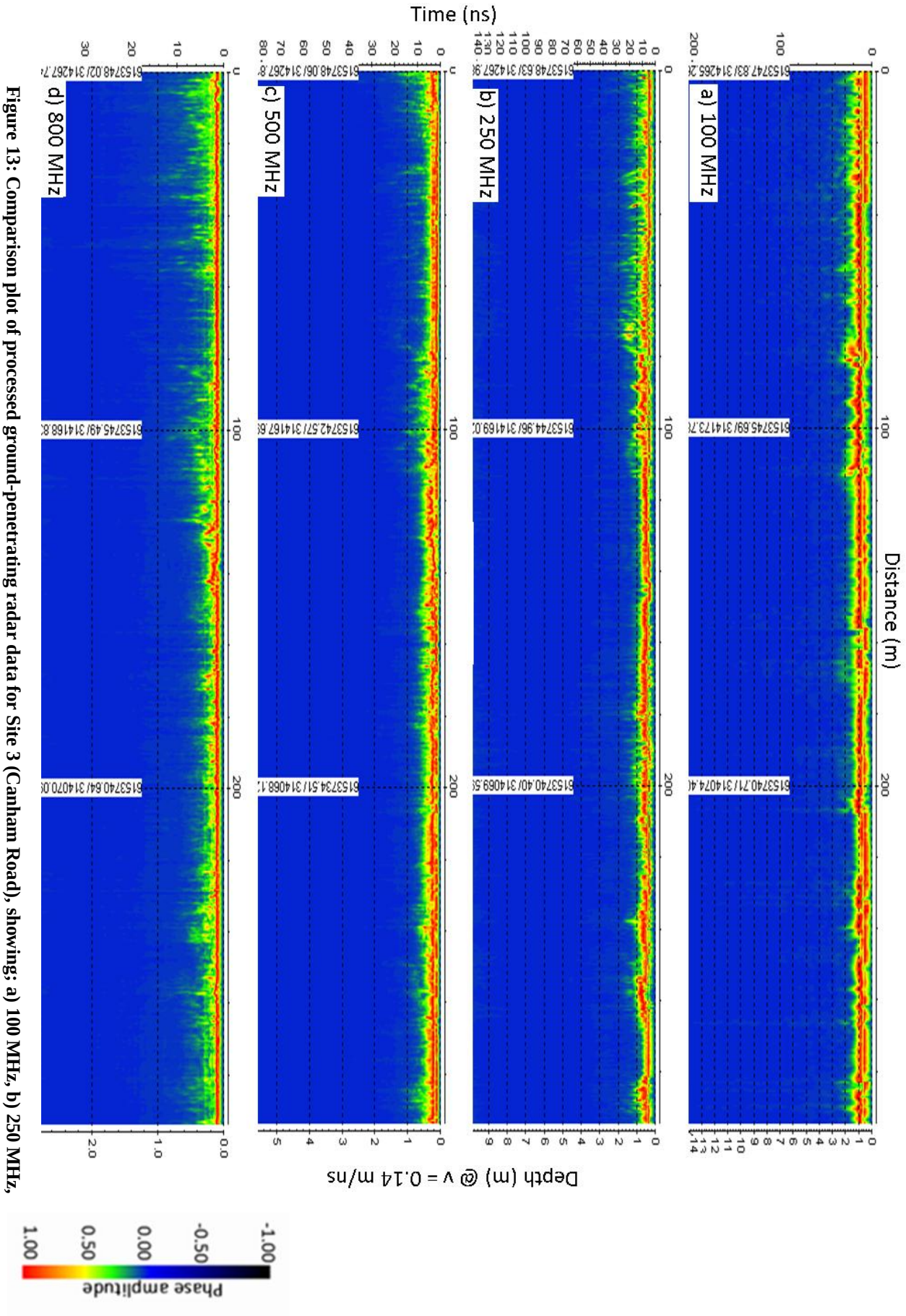

Figure 13: Comparison plot of processed ground-penetrating radar data for Site 3 (Canham Road), showing: a) 100 MHz, b) 250 MHz, c) 500 MHz and d) 800 MHz antenna results. Note that y-axis depth is a function of signal velocity (m/ns) and time (ns). The time windows for each antennae (presented in table 1) dictate the maximum depth of which data can be presented for each antennae.

The GPR estimates from each of the antenna generally show similar patterns regarding reflection locations and penetration depths. Reflectors are detected on all antennae from 0 to 100 m. Higher frequency antennae detect these reflectors further along the profile than lower frequency antennae. Excluding a small scale reflector at 280 meters, no notable reflections are present for all antennae along the rest of the transect. The 500 MHz and 800 MHz antennae show the strongest correlation to one another. The GPR results for all antennae from Site 3 do not reach expected penetration depths. The 800 MHz signal reaches penetration depths ranging from 0.40 to 0.89 m, which are only marginally exceeded by the 250 MHz and 500 MHz antennae. The 100 MHz signal fares slightly better, reaching an approximate depth of 2 m. Due to the limited penetration of depth all antennae, the ability of the 800 MHz antenna to show greater resolution resulted in it being chosen to be further analysed and compared to other geophysical and drilling data sets. The 800 MHz antenna data is presented in a comparative plot with electrical resistivity and DualEM data in Figure 14.

The electrical resistivity (Figure 14a) and DualEM (Figure 14b) results show a general trend of conductive subsurface with minor variations at depth in areas of low topographic relief. A large resistor is present from 15 m east of DH 3.01, to DH 3.06 which among the highest elevation points of the transect. At DH 3.06 there is a contact between the resistive feature and a more conductive part of the section which dominates for the rest of the profile. Shallow resistors are present between DH 3.10 to DH 3.13 and DH 3.16 – DH 3.17. Resistivity readings are typically within 100 – 1000 ohm-m, with highly resistive areas reaching up to 10 000 ohm-m.

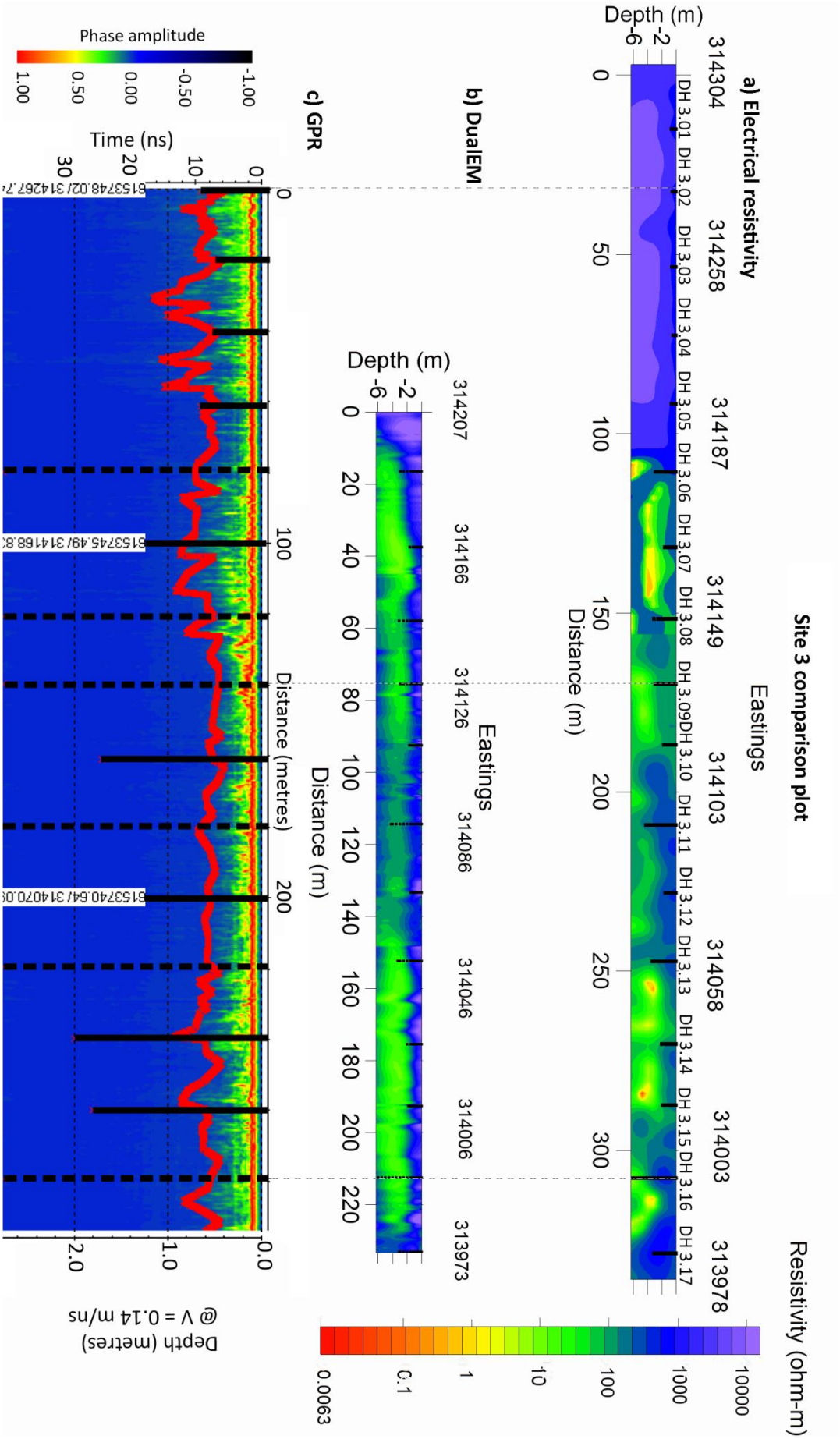

Figure 14: Comparison plot for Site 3, showing: a) electrical resistivity, b) DualEM and c) GPR results. Drill locations and depths are marked on all plots by black lines, with dashed black lines indicating drill depths that exceed the maximum depth of the plot. Estimated GPR bedrock depth is marked on the GPR radargram, represented by a horizontal red line. Plots are aligned by drill hole coordinates. Note that the EM and resistivity results are to a depth of 6 m, compared to GPR radargram depth of ~2.6 metres.

The observed conductive areas rarely reach values below 1 ohm-m. The change from resistive to conductive subsurface has a notable effect on drill refusal depths, as all observed refusal depths below 1 m occurs within resistive areas. These resistive areas also correspond with areas of increased signal penetration depth and reflections in the processed GPR data. The GPR signal outside of the resistive sections shows minor reflections, with extended sections showing zero reflections and complete signal attenuation.

The bedrock depth estimates provided by the 800 MHz GPR antenna at each of the drill locations were compared with the drill refusal depths at the same localities. A paired *t* means test was conducted to test the correlation between the two methods, the results of which are presented in Table 7. A second paired t means test was conducted using drill refusal and GPR bedrock depth estimate data collected at DH 2.08, DH 2.09, DH 2.10 and DH 2.11, which are all located within resistive bodies identified in Figure 14. The results of the second paired *t* means test are presented in Table 8. In the resistive areas the Pearson correlation value is 0.97 which shows a strong correlation between GPR depth estimates and drill refusal results. These results use a small sample size (n = 4) due to the low drill count through the resistive bodies. The Pearson correlation value over the entire survey line (n = 14) is -0.17, showing no correlation between the GPR and drill refusal depths.

Table 7: Paired *t*-test to establish mean value and Pearson correlation between drill refusal depth and GPR bedrock depth estimates at Site 3.

t-Test: Paired Two Sample for Means		All Drill Holes
	Drill	*GPR*
Mean	2.385714286	0.587857143
Variance	2.872472527	0.01711044
Observations	14	14
Pearson Correlation	-0.044734985	

Table 8: Paired *t*-test to establish mean value and Pearson correlation between drill refusal depth and GPR bedrock depth estimates at Site 3, using only data from locations in areas with large scale resistive subsurface.

t-Test: Paired Two Sample for Means		Resistive Areas
	Drill	*GPR*
Mean	1	0.542
Variance	1.13625	0.01352
Observations	5	5
Pearson Correlation	0.793705613	

6. DISCUSSION

The GPR results from all three sites show significantly shallower signal depths than anticipated based upon the theoretical maximum depths of signal penetration presented in Table 1. Radargrams for all antennae show rapid signal attenuation, starting at depths of 0.5 m for the higher frequencies. Lower frequency signals penetrate to greater depths at the cost of vertical resolution, making bedrock contacts unresolvable. Bedrock depth estimations over the three study sites were underestimated by 74% on average. This estimate is derived from both reflection and attenuation depths, depending on radar response. The only exception to this are in select areas with resistive subsurface identified by DualEM and electrical resistivity surveys. At Sites 2 and 3, correlations between GPR bedrock depth estimates over the main resistive units compared to drill

refusal depths were notably improved. The r^2 values at these sites are 0.94 and 0.63 respectively, showing moderate to strong linear trends for GPR depth estimations and drill refusal depths. The resistive areas identified at Site 1 did not prove to influence radar signal in any way. The resistors at this site (~500-1000 ohm-m), are notably less resistive than the resistive zones highlighted at Sites 2 and 3 (~1000-10000 ohm-m). This is an interesting feature of the site that requires further field evaluation.

The electrical resistivity and DualEM results displayed a strong correlation with depth to drill refusal and the top of highly conductive bodies. Most drill holes at Site 2 show refusal at a lateral conductive feature that occurs at 2-4 m depth. Interestingly, some of the drill holes appear to have encountered localised areas where this conductive unit was not as hard and the drill was able to penetrate to greater depths. This is interpreted as a localised change in the geology that is not resolvable with any of the geophysical techniques used. A similar trend is observed at Site 3, where drilling in areas determined by electrical resistivity and DualEM to be highly resistive resulted in refusal depths less than 1 m. Nearby drill holes in conductive areas reached depths of up to 4.7 m at this site. This ambiguity reflects the likelihood that the contacts between overlying soils and bedrock are often not sharp, defined boundaries. Products of bedrock called saprolite form as the bedrock is weathered by chemical and mechanical means. This saprolite forms a fragmented, weathered layer of variable thickness atop of the unweathered bedrock (McDonald & Isbell 2009). The type of bedrock and associated weathering index control the thickness of this saprolitic rock layer (Curmi *et al.* 1994). Materials resistive to chemical weathering, such as quartzite, tend to have thin saprolite layers, while materials more susceptible to chemical weathering tend to have thicker

saprolite layers (Curmi *et al.* 1994). The push-tube percussion drill used for this study is not designed to core through this moderately weathered bedrock (M. Thomas pers. comm. 2013); potentially resulting in imprecise ground truthing data.

6.1 GPR Signal Attenuation

GPR signal attenuation was observed in the radargrams for all antennae frequencies at each site. Olhoeft (1986) identifies signal scattering, soil conductivity and clay content to attribute to GPR signal attenuation. Work by Van Dam *et al.* (2002) and Josh *et al.* (2011) also identify the iron oxide content within soils to also have a profound impact on signal attenuation. These four factors are discussed, relative to the survey results.

6.1.1 SIGNAL SCATTERING

Under favourable conditions GPR surveying has the potential to identify coarse rock fragments (Sucre *et al.* 2010). High concentrations of irregularly shaped coarse fragments can cause signal loss by unpredictable redirection of GPR signal away from the receiver antenna. This type of scattering is common if the incident wavelength is 3 - 10 times smaller than the object. Higher frequency antennae, such as the 500 MHz and 800 MHz used in this study, are more susceptible to signal scattering than lower frequency antennae (Reynolds 1997). Large, coarse fragments that resemble bedrock are more extensive in more developed and extensively weathered profiles. The 100 MHz and 250 MHz antennae showed no increase in reflections where higher frequency antennae show loss of signal. Thus, it is unlikely that signal scattering contributed to the GPR signal attenuation.

6.1.2 SOIL CONDUCTIVITY

The attenuation factor of radar signal, presented in Equations 5 and 6, indicate the main influences of signal attenuation in low-loss soil to be the bulk conductivity and dielectric constant (Reynolds 1997). The loss tangent (*P*) of the soil increases as a function of a materials conductivity (see Equation 2). Features with high conductivity attributes (i.e. lossy soil) cause electromagnetic signal to be converted into thermal energy, which the GPR can no longer measure (Olhoeft 1986). The increase in signal quality within the resistive sections at Sites 2 and 3 suggests that terrain conductivity is attributing to the attenuation of GPR signal. The exception to this is Site 1, in which signal attenuation is observed to have no correlation to conductive areas. The resistors observed at Site 1 are a factor of 10 less resistive than those seen at Site 2 and 3. It is worth nothing that resistivity values at very shallow depths cannot be accurately obtained using the applied EM and electrical resistivity techniques, due to skin depth and resolution factors (Fitterman & Labson 2005). Du and Rummel (1994) found low frequency antennae to be affected by conductive soil conditions to a greater degree than higher frequency antennae. Over all three sites the 100 MHz signal averages a penetration depth of approximately 2 m, instead of the theoretical 10.18 m, showing an 81% underestimation of signal penetration. The antenna shows poor vertical and horizontal resolution at all three sites, with most features rendered undefinable. In comparison the 800 MHz antenna reaches approximately 0.8 m, instead of the theoretical 2.05 m, showing a loss of 61%. This antenna displays high vertical resolution, but still poor horizontal resolution. The poor horizontal resolution suggests that the soil at all three sites are unlikely to be low-loss geological materials for the antennae frequencies used in the survey (Hatch *et al.* 2013). The observed resistivity

values for the conductive areas at the surface are considered to not be low enough to cause the degree of signal attenuation observed at each site. This suggests that while soil conductivity could be a major factor causing signal attenuation, other factors that influence the dielectric constant of the soil, such as moisture, clay content and iron oxide content could be the primary cause of signal attenuation seen across the sites.

6.1.3 CLAY CONTENT

According to Reynolds (1997), the soil velocity (v = 0.14m/ns) is indicative of dry sand (0.12 - 0.17 m/ns) and between wet (86 - 110 m/ns) to dry (173 m/ns) clay. Examination of the soil samples collected at each site shows that the soil profile tends to have dry topsoil; with moisture contents increasing at depths ranging from 0.3 to 0.9 m. These values suggest that signal initially passes through dry sandy soil horizon. The signal then contacts a layer between 0.30 - 0.60 m depth, with a twofold increase in moisture content than that of the dry sand. These depths correspond with observed A and B horizon depths (see Appendix B). The velocity of this layer lies between standard velocities for saturated to dry clay (Reynolds 1997). The presence of clays, particularly with saline groundwater, increases signal attenuation and decreases signal velocity by increasing a soils dielectric constant and bulk conductivity (Doolittle *et al.* 1994, Reynolds 1997). Clays exhibit distinct electrical properties due to their physiochemical structure which includes bound water within its lattice (Reynolds 1997). Clays are also mineralogically unique as they consist of colloidal particles which have an uneven distribution of charge (Olhoeft 1986, Reynolds 1997). Positive charges accumulate within the lattice structure of the clay, while negative charges accumulate on the clays exterior (Olhoeft 1986). The application of an EM field via GPR signal causes the

charge on the clay particles to migrate, converting kinetic energy to thermal energy (Olhoeft 1986). Thermal energy is undetectable by the GPR signal and signal will appear attenuated on a GPR record (Reynolds 1997). Clay-rich, highly conductive soils will yield signal penetration depths of less than 1 m for frequencies as low as 100 MHz (Wright *et al.* 1984). These shallow penetration depths were observed at all three study sites. The presence of clay and increased moisture content at depth observed at each site provides an explanation of the attenuation of GPR signal. Further work to quantify the clay content of the soils needs to be conducted before the overall effect of this factor can be determined.

6.1.4 IRON OXIDE CONTENT

Van Dam *et al.* (2002) demonstrated that the presence of iron oxide as precipitates does not directly influence the three components of electromagnetic waves (μ, σ and ε). Thus, the concentration of iron oxide does not alter the relative dielectric permittivity of a sediments solid phase (Mätzler 1998). Iron oxides only have an influence on the dielectric permittivity of a soil when water is present (Van Dam *et al.* 2002). The amount of iron oxide present within a material correlates to volumetric water content (Van Dam *et al.* 2002). This correlation is caused by the capillary retention capacity of iron oxides compared to other minerals. As previously discussed, the soil moisture content of the soils at each site increased with depth. This increase has the potential to correlate to increased dissolved iron oxides within the soil profiles, contributing to signal attenuation. Josh *et al.* (2011) discovered iron oxide concentrations of 0.4% wt. within favourable GPR survey conditions to reduce 250 MHz signal penetration depth from 10 m to below 1 m. The iron oxide minerals in this study occurred within a clay

coating on quartz grains, along with subsidiary amounts of kaolin, carbonates and smectite (Josh *et al.* 2011). It is worth noting that the soils observed at Site 3 were logged as ferruginous due to their red hue, while soils at Sites 1 and 2 not displaying this feature. Without quantifying if dissolved iron oxide occurred in the horizons, or as inclusions within clay coatings on grains, the exact influence of iron oxides on the dielectric properties of the soils at the study sites, if any, cannot be identified. Thus, the role of iron oxides as a contributor to the observed signal attenuation cannot be determined.

6.2 Signal attenuation summary

Considering all these factors, it is determined that signal scatter is unlikely to have occurred at any of the sites. The cause of attenuation has been narrowed to ground conductivity, clay content and iron oxide presence. These factors all tend to have an increased chance of occurring within a soils B horizon (Doolittle & Collins 1995). The average B horizon ranges at each site are as follows: Site 1 ≅ 0.36 - 0.91 m depth, Site 2 ≅0.23 - 0.85 m depth and Site 3 ≅ 0.18 - 1.30 m depth. The B horizon was present throughout Site 1, with subsurface conductivity sharing no relation to thickness of the horizon. Site 2 and 3 demonstrated the thickness of the B horizon to be negatively influenced by the presence of resistive subsurface features. The B horizon was on average between 0.0 – 0.15 m thick in areas where resistors were present. GPR signal in these areas penetrated to greater depths and provided more accurate bedrock depth estimates when compared to drilling results. The direct correlation between B horizon presence and signal attenuation at all three sites could be attributed to conductive, lossy soil conditions with increased iron oxide and clay presence in the B horizon amplifying

signal attenuation. Without further in-depth analysis of these factors, it is difficult to make a solid conclusion regarding the primary cause of this signal attenuation.

7. CONCLUSIONS

The type of terrain in which data are collected is highly influential to the practical applicability of GPR, with soil type, moisture and conductivity all having potentially severe impacts on the quality of collected data. In the instance of Adelaide Hills-type soils found at Mount Crawford, this study has shown GPR to be relatively ineffective. Signal attenuation greatly affected the signal penetration depth and clarity at all three sights. The cause of attenuation is speculated to be caused by the clay contents, iron oxide contents and bulk conductivities of the investigated soils. These factors typically increase in value within B horizon soils, in which all observed signal attenuation occurred. It is likely that a combination of all three of the above factors caused the signal loss. The system showed increased estimation accuracy in areas with highly resistive subsurface detected by electrical resistivity and EM surveys; though sample sizes in these areas were small, and the results were not consistent across all three sites. The tendency of weathered terrains to have more developed B horizons leads to the recommendation of using other geophysical methods, such as electrical resistivity, in Adelaide Hills-type environments. An explicit knowledge of the soil properties in the target terrain is advantageous, thus local soil studies should be considered in these types of environments before the application of a GPR survey.

8. ACKNOWLEDGMENTS

I would like to thank Michael Hatch for his constant support, comments and role as project supervisor throughout the year. I would also like to thank Mark Thomas and John Wilford from the CSIRO and Geoscience Australia for research funding and support. I would like to thank John Triantafilis and Thomas Fotheringham for data collection assistance, processing EM and resistivity data, and providing valuable comments. Thanks to David Hamilton-Smith, Kate Robinson and Sebastian Schnaidt for assistance in the field. Thanks to Jingping Zhe, Phil Mill, and Mads Toft for assistance with processing software. Thanks also to Katie Howard for organising project deadlines and support throughout the year. Finally, thanks to Lars Krieger for help with thesis drafting and editing.

9. REFERENCES

ANNAN A. P. 2005. Ground-Penetrating Radar. *In:* Butler D. K. ed., *Near-Surface Geophysics*, Vol. Investigations in Geophysics, pp 357-438, Society of Exploration Geophysicists.

BANTON O., SEGUIN M. K. & CIMON M. A. 1997. Mapping field scale physical properties of soil with electrical resistivity. *Soil Sci. Soc. Am. J.* **61**, 1010-1017.

BENBOW M. C., ALLEY N. F., CALLEN R. A. & GREENWOOD D. R. 1995. Geological history and palaeoclimate. *In:* Drexel J. F. & Preiss W. V. eds., *The geology of South Australia*, Vol. 54, pp 208-217, Geological Survey of South Australia Bulletin.

BLACKBURN G. 1958. *Soil Mapping in the Mt. Crawford Forest Reserve, South Australia*. *Technical Memo*. CSIRO Division of Soils.

BOURMAN R. P. & LINDSAY J. M. 1989. *Timing, extent and characted of Late Cainozoic Faulting on the eastern margin of the Mt Lofty Ranges, South Australia*. **113:** 63-67. Royal Society of South Australia.

CAI J. & MCMECHAN G. A. 1995. Ray-based synthesis of bistatic ground-penetrating radar profiles. *Geophysics* **60**, 87-96.

CARCIONE J. M. 1996. Ground-penetrating radar: wave theory and numerical simulation in lossy anisotropic media. *Geophysics* **61**, 1664-1677.

CHANZY A., TARUSSOV A., JUDGE A. & BONN F. 1996. Soil water content determination using a digital ground-penetrating radar. *Soil Sci. Soc. Am. J.* **60**, 1318-1326.

CHARLTON M. B. 2008. *Principles of ground-penetrating radar for soil moisture assessment*. Walker institute for Climate System Research, University of Reading.

COLLINS M. E. & DOOLITTLE J. A. 1987. Using ground penetrating radar to study soil microvariability. *Soil Sci. Soc. Am. J.* **51**, 491-493.

CONOR C. H. H. 1984. Draft report, Williamstown industrial mineral deposits. Geology of koalin-sillimanite-muscovite deposits, near Williamstown, Hd. Barossa, Mt. Lofty Ranges, South Aust. *Department of Primiary Industries and Resources South Australia Report Book 84/65*.

COULOUMA G., SAMYN K., GRANDJEAN G., FOLLAIN S. & LAGACHERIE P. 2011. Combining seismic and electric methods for predicting bedrock depth along a Mediterranean soil toposequence. *Geoderma* **170**, 39-47.

COULOUMA G., TISSEYRE B. & LAGACHERIE P. 2010. Is a Systematic Two-Dimensional EMI Soil Survey Always Relevant for Vineyard Production Management? A Test on Two Pedologically Contrasting Medieterranean Vineyards. *In:* Viscarra Rossel R. A., McBratney A. & Minasny B. eds., *Proximal Soil Sensing. Progress in Soil Science series*, pp 283-295, Springer, New York.

CURMI P., WIDIATMAKA, PELLERIN J. & RUELLAN 1994. Saprolite influence on formation of well-drained hydromorphic horizons in an acid soil system as determined by structural analysis. *Developments in Soil Science* **22**, 133-140.

DAILY B., FIRMAN J. B., FORBES B. G. & LINDSAY J. M. 1976. Geology. *In:* Twidale C. R. T., Tyler M. J. & Webb B. P. eds., *Natural History of the Adelaide Region*, Royal society of South Australia Inc.

DAVIS J. L. & ANNAN A. P. 1989. Ground-penetrating radar for high-resolution mapping of soil and rock stratigraphy. *Geophysical Prospecting* **37**, 531-551.

DOOLITTLE J. A. & COLLINS M. E. 1995. Use of soil information to determine application of ground penetrating radar. *Journal of Applied Geophysics* **33**, 101-108.

DOOLITTLE J. A., SUDDUTH K. A., KITCHEN N. R. & INDORANTE S. J. 1994. Estimating depths to claypans using electromagnetic induction methods. *J. Soil and Water Cons* **49**, 572-575.

DU S. & RUMMEL P. 1994. Reconnassance studies of moisture in the subsurface with GPR. *Proceedings of the Fifth International Conference on Ground Penetrating Radar,* Kitchener, Ontario, pp. 1241-1248.

FITTERMAN D. V. & LABSON V. F. 2005. Electromagnetic Induction Methods for Environmental Problems. *In:* Butler D. K. ed., *Near-Surface Geophysics*, Vol. Investigations in Geophysics, pp 301-356, Society of Exploration Geophysicists.

FITZPATRICK E. A. 1988. Soil Horizon Designation and Classification. *International Soil Reference and Information Centre*.

FORESTRYSA 2006. Little Mount Crawford Native Forest Reserve Management Plan. *Forestry SA*.

GEONICS LIMITED 2013. DUALEM-421s User Guide.

GRIFFIN S. & PIPPET T. 2002. Ground Penetrating Radar. *CRCLEME Open File Report Geophysical and Remote Sensing Methods for Regolith Exploration*.

HATCH M., HEINSON G., MUNDAY T., THIEL S., LAWRIE K., CLARKE J. D. A. & MILL P. 2013. The importance of including conductivity and dielectric permittivity information when processing low-frequency GPR and high-frequency EMI data sets. *Journal of Applied Geophysics* **96**, 77-86.

JACKSON E. A. 1957. *A survey of the soils and their utilisation in portion of the Mt. Lofty Ranges, South Australia*. *Soils and Land Use Service*. **21**. CSIRO Division of Soils.

JOL H. M. & BRISTOW C. S. 2003. An introduction to ground penetrating radar (GPR) in sediments. *In*, *Ground penetrating radar in sediments*, Vol. 211, pp 1-7, Geological Society Special Publications, London.

JOL H. M. & SMITH D. G. 1991. Ground penetrating radar of northern lacustrine deltas. *Can. J. Earth Sci.* **28**, 1939-1947.

JOSH M., LINTERN M. J., KEPIC A. W. & VERRAL M. 2011. Impact of grain-coating iron minerals on dielectric response of quartz sand and implications for ground-penetrating radar. *Geophysics* **76**, J27-J34.

KEAREY P., BROOKS M. & HILL I. 2002. *An introduction to geophysical exploration*. Blackwell Science.

MALA GEOSCIENCE 2013. X3M control unit user manual.

MÄTZLER C. 1998. Microwave permittivity of dry sand. *IEEE Trans. Geosci. Remote Sensing* **36**, 317-319.

MCDONALD R. C. & ISBELL R. F. 2009. Soil Profile. *In*, *Australian Soil and Land Survey Field Handbook*, pp 147-200, CSIRO, Melbourne.

MCNEILL J. D. 1990. Use of Electromagnetic Methods for Groundwater Studies. *In:* Ward S. H. ed., *Geotechnican and Environmental Geophysics*, Vol. Volume 1: Review and Tutorial, Anacortes, Washington, US.

MCNIELL J. D. 1980. Applications of Transient Electromagnetic Techniques. *Geonics Limited*.

MONTEIRO SANTOS F. A., TRIANTAFILIS J., BRUZGULIS K. E. & ROE J. A. E. 2009. Inversion of DUALEM-421 profiling data using a 1-D laterally constrained algorithm. *Vadose Zone Journal* **9**, 117-125.

OLHOEFT G. R. 1986. Direct detection of hydrocarbon and organic chemicals with ground penetrating radar and complex resistivity. *NWWA/API Conference on Petroleum, Hydrocarbons and Organic Chemicals in Ground Water - Prevention, Detection and Restoration*.

PREISS W. V. 1987. Basement inliers of the Mount Lofty Ranges. *In*, *The geology of South Australia, Volume 1, The Precambrian*, pp 102-105, Geological Survey of South Australia, Adelaide.

PREISS W. V., FANNING C. M., SAPUNAR M. A. & BURTT A. C. 2008. Age and tectonic significance of the Mount Crawford Granite Gneiss and a related intrusive in the Oakbank Inlier, Mount Loft Ranges, South Australia. *MESA Journal* **49**, 38-40.

REYNOLDS J. M. 1997. *An Introduction to Applied and Environmental Geophysics*. Wiley, Chichester.

SAARENKETO T. 1998. Electrical properties of water in clay and silty soils. *J. Appl. Geophys.* **40**, 73-88.

SAMOUELIAN A., COUSIN I., TABBAGH A., BRUAND A. & RICHARD G. 2004. Electrical resistivity survey in soil science: a review. *Soil & Tillage Research* **83**, 173-193.

SANDIFORD M. 2002. Neotectonics of southeastern Australia: linking the Quaternary faulting record with seismicity and in situ stress. *Geological Society of Australia Special Publication* **22**.

SUCRE E. B., TUTTLE J. W. & FOX T. R. 2010. The use of ground-penetrating radar to accurately estimate soil depth in rocky forest soils. *Forest Science* **57**, 59-66.

TELFORD W. M., GELDART L. P., SHERIFF R. E. & KEYS D. A. 1990. *Applied Geophysics* (2nd edition). Cambridge University Press, Cambridge.

TOKAREV V. 2005. Neotectonics of the Mount Lofty Ranges (South Australia). PhD thesis, School of Earth & Environmental Sciences, Geology & Geophysics, The University of Adelaide, Adelaide (unpubl.).

TOKAREV V. & GOSTIN V. 2003. *Mt Lofty Ranges, South Australia*. *Regolith-Landscape Evolution Across Australia*. Anand R. R. & De Broekert P. Cooperative Research Center for Landscape Evolution and Mineral Exploriation, Canberra.

TOWNSEND I. J. 1984. Williamstown clay mine, a unique deposit? *South Australia Department of Mines and Energy South Australia - Exploration Potential*.

TRIANTAFILIS J. & BUCHANAN S. M. 2009. Identifying common near-surface and subsurface stratigraphic units using EM34 signal data and fuzzy k-means analysis in the Darling River valley. *Australian Journal of Earth Sciences* **56**, 535-558.

TRIANTAFILIS J., TERHUNE IV C. H. & MONTEIRO SANTOS F. A. 2013. An inversion approach to generate electromagnetic conductivity images from signal data. *Environmental Modelling and Software* **43**, 88-95.

VAN DAM R. L., SCHLAGER W., DEKKERS M. J. & HUISMAN J. A. 2002. Iron oxides as a cause of GPR reflections. *Geophysics* **67**, 536-545.

WIGHTMAN W. E., MARTINEK B. C. & HAMMERMEISTER D. 1992. Geophysical Methods Used to Guide Hydrogeological Investigations at an Umtra Site Near Grand Junction, Colorado. *In:* Nielsen D. M. & Sara M. N. eds., *Current Practices in Ground Water and Vadose Zone Investigations*, American Society for testing and Materials, Philadelphia.

WILFORD J. & THOMAS M. 2012. Modelling soil-regolith thickness in complex weathered landscapes of the central Mt Lofty Ranges, South Australia. *Digital Soil Assessments and Beyond,* Sydney, Australia, pp. 69-75. Taylor and Francis Group.

WRIGHT D. L., OLHOEFT G. R. & WATTS R. D. 1984. Ground-penetrating radar studies on Cape Cod. *In:* Nielsen D. M. ed., *Surface and borehole geophysical methods in groundwater investigations*, pp 666-680, Nat. Water Well Assoc., Worthington, OH.

ZHE J., GREENHALGH S. A. & MARESCOT L. 2007. Multichannel, full waveform and flexible electrode combination resistivity-imaging system. *Geophysics* **72**, 57-64.

ZHOU B. & GREENHALGH S. A. 1999. Explixit expressions and numerical calculations for the Frechet and second derivatives in 2.5D Helmholtz equation inversion. *Geophysical Prospecting* **47**, 443-468.

ZONGE K., WYNN J. & URQUHART S. 2005. Resistivity, Induced Polarization and Complex Resistivity. *In:* Butler D. K. ed., *Near-Surface Geophysics*, Vol. Investigations in Geophysics, pp 265-300, Society of Exploration Geophysicists.

APPENDIX A:

DETAILED METHODS

Ground Penetrating Radar

Equipment/application: A MALÅ geoscience X3M GPR control unit and MALÅ XV monitor was used with 100 MHz, 250 MHz, 500 MHz and 800 MHz fixed-separation shielded antennae, mounted on a rough terrain push cart. The traverses at each site were based upon the drilling locations, with the GPR track passing approximately 20cm to the right of each of the drill holes. At each site the required settings for the antennae were set as observed in Table 1. Data were collected a total of 4 times at each site per antennae.

Antennae	100 MHz	250 MHz	500 MHz	800 MHz
Time Window	198.6 ns	140.0 ns	78.8 ns	39.6 ns
Theoretical Max Depth	10.18 m	7.18 m	4.03 m	2.05 m
Point/Time Interval	0.25 s	0.05 m	0.04 m	0.019 m
Samples Per Interval	344	536	624	512
Sampling Frequency	1581.25 MHz	3614.29 MHz	7535.71 MHz	12173.08MHz
Antennae fixed offset	0.5 m	0.36 m	0.18 m	0.14 m

Table 1: GPR settings

The traverses using the GPR were made travelling in forward and reverse directions twice, giving a total of 4 traverse files to be used for analysis. All GPR data have been taken assuming vertical incidence due to the small antennae spacings. A differential GPS was attached to the GPR system allowing coordinates to be recorded into the data file.

Processing: The raw data were imported and processed as follows:

1) Raw data file imported into Reflex W using RAMAC GPR settings
2) Raw data associated with .COR file containing GPS coordinates
3) Coordinates converted to WGS 84 zone54s
4) Subtract mean (DeWow) 1D filter removed any DC offset
5) Static correction by manual picking of the first positive phase arrival to remove air wave.
6) Background removal filter was applied to remove all background noise and present a truer signal
7) Wave velocity determined by hyperbola reflection analysis, giving a depth function of 0.14 m/ns
8) F-K migration (Stolt) was applied using a velocity function of 0.14 m/ns to reduce hyperbola presence and present a truer image of subsurface features
9) Enveloping of the signal, converting negative phase data into a positive phase
10) 2D running average filter applied to each transect acted as a smoothing filter for final presentation and result interpretation. Traces averages used for each antenna

were as follows: 100 MHz – 5 traces, 250 MHz – 10 traces, 500 MHz – 20 traces, 800 MHz – 40 traces.

The below figure presents a typical processing flow from a fully filtered data set.

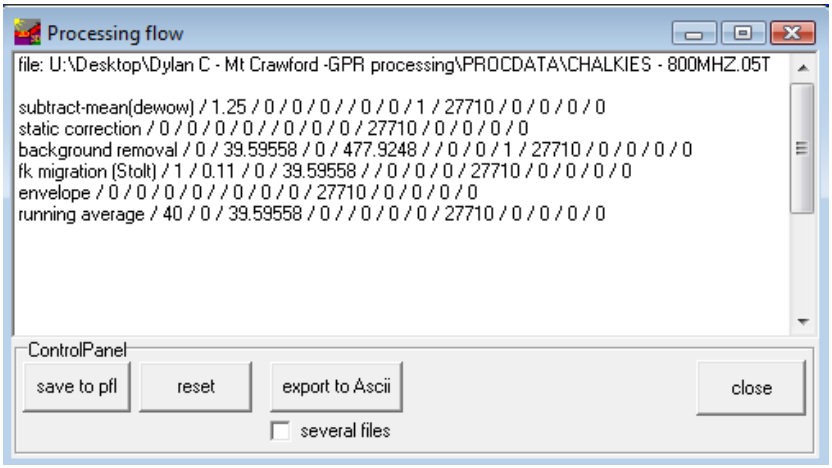

Full detailed explanations of the applications for each filtering step are available in the ReflexW user guide. Note that gain functions were not applied to any data sets as many became distorted, even at low decibel increases.

Following processing, location and depth of each drill hole was manually picked based upon the GPS coordinates. Bedrock depth estimations were made using a phase follower picking method with a tolerance of +0.25 amplitude. This was initially picked manually in resistive zones where bedrock depth estimations were most accurate. The phase follower automatically picked the remained of the data and created a bedrock estimate layer. This layer was viewed manually to determine if the picks corresponded to bedrock reflections, or to signal attenuation. Visual analysis of each antennae established the frequency that produced the most accurate bedrock estimates.

Data were exported into a .bmp file format for final presentation.

Electrical Resistivity

Equipment Application: DC 2D electrical resistivity surveys were undertaken in the field using a ZZ Resistivity Imaging FlashRES-64 system along each of the three traverses. Each spread of the resistivity instrumentation consisted of 64 electrodes with 1.5 meter spacing. The transmitter/receiver was located in a central location along the spread, with 32 electrodes on either side. Each electrode was hammered to approximately 10-15 cm depth, ensuring good contact with soil. One earthing electrode was placed near the transmitter/receiver and connected to the grounding input. A salt water mixture was created by mixing 1 kg of salt into a 20 L container of fresh water. Each electrode was covered by approximately 50-100 ml of this salt water mixture. A cable designed to connect the electrodes to the transmitter/receiver was placed and each electrode was connected to its corresponding location along the cable, which was then connected to the transmitter/receiver. The control box was connected to a 12V car

battery and a laptop. The laptop was used to run the FlashRES-64 operating program and test the connectivity of each electrode.

The survey parameters were set as observed in Table 2 and the survey was run. Upon completion of the survey the cables were disconnected and electrodes removed, with the entire system being moved along the transect. There was a 14 electrode overlap between spreads, and a 14 electrode overlap of the beginning and end of the transects.

Survey Type	Output	Input Channels	Electrode Spacing	Sampling Interval	Start Electrode	End Electrode
Resistivity	120 V @ 250 W (240 V per pair)	61 channels	1.5 meters	3 seconds	0	64

Table 2 – Electrical resistivity survey settings

Processing: Data were inverted using a 2.5D Helmholtz inversion equation. All inverted data were loaded into surfer gridding software and produced on a basic grid using a logarithmic scale. All processing was completed externally. A full explanation of the system and inversion codes are available in (Zhou & Greenhalgh 1999, Zhe *et al.* 2007)

Electromagnetics

Equipment Application: A Geonics DualEM-421s frequency-domain system was used for EM surveying at each site. The DualEM-421s consists of 3 pairs of horizontal co-planar (HCP) and perpendicular (PRP) orientated receiver arrays (Geonics Limited 2013)A singular transmitter is shared by all arrays, operating at a frequency of 9 kHz. The DualEM survey involved carrying the instrument along each traverse at a height of 0.30 m, using drill hole locations and a differential GPS to provide geo-referencing.

Processing: DualEM data inversion were completed externally using EM4Soil Monteiro Santos *et al.* (2009) and Triantafilis *et al.* (2013) describe algorithms and software used for data inversion. The Krieging method was used in Surfer gridding software to present the inverted data in a logarithmic scale.

All inverted EM and electrical resistivity results were combined in surfer software using co-ordinates to align each data set. GPR data were exported and manually placed on each comparison plot using drill location coordinates to align with the other data sets.

Soil Analysis

The soil collected from each drill hole was analysed for the purpose of cross comparison with the applied geophysical techniques. Often techniques will not perform as initially anticipated in the field and soil analysis results will help to explain why certain techniques show good quality data, while others may not. Anomalies and errors related to equipment operation can also be mitigated by comparison with associated soil data.
4.4.1 Application: Each transect was marked with 20m intervals, which were used to determine the drill sites. Push tube percussion drilling was used to drill to a maximum depth of 9m, or to drill refusal. Removed samples were gathered and sub-sampled into 30cm depth intervals from 0cm to 150cm, and in 50cm depth intervals from 150cm to drill refusal depth. Each sample bag was weighed in the field using a scale to obtain the wet weight of the soil. The extent of weathering of each soil sample was described and recorded.
The sample bags were labelled and placed into an oven for 2 weeks. Upon completion of the drying process, the same scale was used to re-weigh the samples, giving an absolute value for the moisture content of the soil. Each of the dry samples were separated into two fractions using a 2 mm sieve. The >2 mm fractions were weighed and set aside, as were the <2 mm fractions. 5 grams of the <2mm fraction was removed and used for EC 1:5 salinity analysis. EC 1:5 analysis consisted of weighing exactly 5 grams of <2 mm soil to 25 grams distilled water, placing on a rotating drum at 25 rpm for 1 hour. The samples were left to settle for 30 minutes before the EC 1:5 readings were taken. A K=10 electrode was used for measurements in each sample and rinsed with RO water between each reading. This method is further detailed in: Rayment, G.E., Higginson, F.R., 1992. Australian laboratory handbook of soil and water chemical methods. Australian Soil and Land Survey Handbook. Inkata Press, Melbourne.

All results were recorded and presented in excel spreadsheets.

APPENDIX B:

SOIL ANALYSIS DATA

Site 1: Rocky Paddock								
Drill Hole	**Distance Along Line (metres)**	**Coordinates Easting**	**Northing**	**Total Drill Depth**	**soil depth increment**	**Moisture wt. %**	**E:C 1.5 µs/cm**	**Soil Horizon**
1.01	0	311270	6156095	1.5	00/30	7.14	81.00	
					30/60	10.97	58.10	
					60/90	3.38	39.10	
					90/120	-0.42	30.20	
					120/150	-0.93	34.70	
1.02	20	311258	6156079	1.5	00/30	1.95	113.70	
					30/60	8.93	65.70	
					60/90	2.33	43.20	
					90/120	8.54	61.30	
					120/150	3.96	76.60	
1.03	40	311244	6156064	1.9	00/30	3.51	83.00	
					30/60	7.94	50.40	
					60/90	6.67	37.20	
					90/120	10.90	50.00	
					120/150	7.45	51.50	
					150/190	6.43	43.00	
1.04	60	311230	6156051	1.35	00/30	-0.17	81.30	A
					30/60	7.35	47.20	B
					60/90	3.49	31.80	C
					90/120	3.24	29.00	C
					120/135	2.71	38.70	C
1.05	80	311215	6156038	1.5	00/30	3.86	199.80	A

					30/60	13.01	53.10	B
					60/90	9.83	39.00	C
					90/120	2.88	26.60	C
					120/150	3.18	33.50	C
1.06	100	311201	6156024	1.8	00/30	1.51	100.60	A
					30/60	11.99	58.00	B
					60/90	14.01	48.10	B
					90/120	10.04	40.40	C
					120/150	5.54	33.50	C
					150/180	4.77	28.70	C
1.07	120	311185	6156011	2	00/30	2.86	107.40	A
					30/60	7.78	55.90	B
					60/90	12.97	48.50	B
					90/120	7.58	34.20	B
					120/150	5.98	35.60	C
					150/200	7.60	34.20	C
1.08	140	311170	6155999	2	00/30	1.48	70.20	A
					30/60	4.41	45.30	A2
					60/90	15.76	58.40	B
					90/120	N/A	58.20	B
					120/150	11.99	55.10	C
					150/200	7.27	41.80	C
1.09	160	311155	6155987	4.7	00/30	1.83	135.60	
					30/60	13.16	60.50	
					60/90	12.35	57.10	
					90/120	12.49	60.40	
					120/150	2.96	38.60	

					150/200	7.67	31.20	
					200/250	11.56	34.80	
					250/300	18.15	76.20	
					300/350	16.34	90.60	
					350/400	16.46	123.90	
					400/450	11.24	100.00	
					450/470	9.21	117.00	
1.10	180	311139	6155973	1.2	00/30	3.12	138.40	A
					30/60	4.28	51.90	A2
					60/90	9.72	62.20	B/C
					90/120	11.90	62.30	R
1.11	200	311124	6155961	3.3	00/30	1.31	108.90	A
					30/60	13.29	63.10	B2
					60/90	15.23	68.30	B2
					90/120	11.34	61.30	B2
					120/150	10.98	58.40	B2
					150/200	10.61	60.40	C
					200/250	10.91	55.40	C
					250/300	11.46	44.90	C
					300/330	6.67	76.00	C
1.12	220	311108	6155948	1.5	00/30	2.31	183.20	A
					30/60	10.05	104.80	B
					60/90	12.38	76.90	B
					90/120	11.34	75.40	R
					120/150	8.94	92.40	R
1.13	240	311093	6155937	3	00/30	2.20	104.80	A
					30/60	13.64	104.00	B2

					60/90	8.54	59.30	B2
					90/120	5.63	99.30	C
					125/150	7.40	151.10	C
					150/170	3.85	97.00	C

Site 2: Chalkies Line								
2.01	0	312622	6153444	1.9	00/30	11.83	121.50	A
					30/60	13.64	78.30	B2
					60/90	11.79	140.10	C
					90/120	11.46	231.00	R
					120/150	14.19	287.00	R
					150/190	14.55	346.00	R
2.02	20	312641	6153440	1.7	00/30	7.06	150.00	A
					30/60	12.49	69.30	B
					60/90	9.12	69.90	C
					90/120	8.63	102.90	R
					120/150	6.89	171.90	R
					150/170	4.51	143.80	R
2.03	33	312653	6153446	4.8	00/30	4.13	92.60	A
					30/60	11.41	65.10	B2
					60/90	7.51	55.10	B2
					90/120	3.27	41.40	C
					120/150	2.94	46.70	C
					150/200	2.65	108.00	R
					200/250	5.13	176.50	R
					250/300	8.14	156.20	R

					300/350	10.53	84.10	R
					350/400	11.07	94.10	R
					400/450	8.39	79.70	R
					450/480	7.57	68.50	R
2.04	40	312660	6153442	1.45	00/30	5.07	67.80	A
					30/60	11.02	48.10	B
					60/90	7.01	40.80	B
					90/120	5.22	43.80	C
					120/145	5.56	66.10	R
2.05	60	312680	6153437	2.4	00/30	2.94	93.00	A
					30/60	9.99	121.00	B2
					60/90	7.35	65.10	C
					90/120	4.99	34.40	C
					120/150	5.18	42.10	C
					150/200	3.86	38.00	C
					200/240	2.52	26.30	R
2.06	80	312699	6153439	7.3	00/30	5.57	57.30	A
					30/60	7.51	38.30	A2
					60/90	11.45	36.00	B2
					90/120	2.80	25.40	C
					120/150	2.67	33.80	C
					150/200	6.32	79.00	C
					200/250	7.10	44.60	C
					250/300	8.09	48.20	C
					300/350	7.21	45.70	C
					350/400	5.96	43.00	C
					400/450	6.68	47.90	C

					450/500	9.64	67.00	C
					500/550	9.71	75.80	C
					550/600	11.98	86.30	C
					600/650	11.07	85.80	C
					650/700	10.69	80.80	C
					700/730	8.47	69.80	C
2.07	100	312721	6153433	5.9	00/30	6.26	70.00	A
					30/60	13.93	65.40	B2
					60/90	8.72	34.60	C
					90/120	5.78	28.10	C
					120/150	2.98	30.00	C
					150/200	3.13	26.20	C
					200/250	2.95	29.10	C
					250/300	5.77	31.40	C
					300/350	6.48	27.40	C
					350/400	6.83	24.10	C
					400/450	6.56	26.10	C
					450/500	6.44	27.60	C
					500/550	7.14	30.00	C
					550/590	8.46	27.00	C
2.08	120	312740	6153435	0.8	00/30	1.17	34.60	A
					30/60	2.84	31.20	C
					60/80	3.53	31.40	C/R
2.09	140	312759	6153439	0.95	00/30	3.24	36.90	A
					30/60	5.06	36.50	B
					60/95	9.49	43.30	C
2.10	160	312779	6153436	5.2	00/30	5.44	46.60	

					30/60	13.31	45.30	A
					60/90	10.82	30.90	B
					90/120	11.33	32.30	B
					120/150	10.78	36.20	B
					150/200	7.02	32.20	C
					200/250	10.94	31.10	C
					250/300	13.17	44.30	C
					300/350	12.80	34.10	C
					350/400	11.75	29.90	C
					400/450	13.64	30.90	C
					450/500	12.88	33.00	C
					500/520	11.90	40.80	R
2.11	180	312798	6153437	0.8	00/30	4.17	47.30	A
					30/60	8.19	33.50	B
					60/80	7.29	30.10	R
2.12	200	312817	6153439	1.4	00/30	3.58	72.80	A
					30/60	12.34	46.30	B1
					60/90	11.78	39.00	B2
					90/120	10.88	45.60	C
					120/140	10.23	56.10	R
2.13	220	312834	6153432	2.25	00/30	3.71	59.40	A
					36/60	11.36	42.90	B2
					60/90	12.40	34.60	B2
					90/120	8.78	30.40	B2
					120/150	8.57	35.40	C
					150/200	12.23	64.20	C
					200/225	10.94	53.20	R

2.14	240	312859	6153431	2.3	00/30	2.50	46.30	A
					30/60	7.42	32.10	B2
					60/90	10.86	32.60	B2
					90/120	4.92	34.20	B2
					120/150	3.60	31.90	C
					150/200	4.35	47.60	C
					200/230	6.50	39.50	C
2.15	260	312879	6153430	1.35	00/30	4.93	57.90	A
					30/60	9.89	38.30	B
					60/90	10.63	47.20	B
					90/120	7.68	47.60	C
					120/135	7.84	73.40	C
2.16	280	312898	6153426	7.15	00/30	2.27	54.20	A
					30/60	9.35	40.60	B2
					60/90	8.65	36.10	B2
					90/120	8.28	36.30	C
					120/150	5.95	42.50	C
					150/200	5.60	49.90	C
					200/250	10.63	63.90	C
					250/300	13.75	88.60	C
					300/350	14.13	88.70	C
					350/400	13.57	115.70	C
					400/450	17.44	114.30	C
					450/500	17.26	108.60	C
					500/550	16.15	94.70	C
					550/600	18.29	115.70	C
					600/650	17.55	124.40	C

					650/700	19.28	121.10	C
					700/715	19.25	125.50	C
2.17	300	312917	6153429	0.85	00/30	10.19	66.70	A/B
					30/60	9.35	42.60	B2
					60/85	9.51	58.50	B2/C
2.18	320	312938	6153428	1.05	00/30	10.15	97.10	A
					30/60	15.15	62.20	B2
					60/90	10.58	61.40	B2
					90/105	9.68	72.00	C
2.19	340	312958	6153427	3.3	00/30	8.20	61.40	A/B
					30/60	14.85	44.50	B
					60/90	12.23	40.10	B
					90/120	12.96	41.40	B
					120/150	13.81	52.50	C
					150/200	17.21	65.80	C
					200/250	18.42	82.20	C
					250/300	12.72	89.60	C
					300/330	13.22	128.50	C
2.2	360	312978	6153426	1.5	00/30	4.58	45.20	A1
					30/60	7.71	50.60	B1
					60/90	13.53	43.40	B2
					90/120	8.84	41.20	C
					120/150	9.88	52.40	C/R
2.21	400	313019	6153422	1.5	00/30	5.09	52.80	
					30/60	16.41	60.20	
					60/90	17.28	63.10	
					90/120	16.80	76.60	

					120/150	15.82	129.50	
2.22	460	313079	6153420	6	00/30	3.54	70.80	A
					30/60	7.90	61.60	B
					60/90	9.99	61.80	B
					90/120	9.73	56.70	C
					120/150	9.59	79.80	C
					150/200	13.76	251.00	C
					200/250	8.49	231.70	C
					250/300	9.42	449.00	C
					300/350	9.46	N/A	C
					350/400	10.79	539.00	C
					400/450	8.98	430.00	C
					450/500	13.00	610.00	C/R
					500/550	13.48	610.00	R
					550/600	9.94	416.00	R
2.23	560	313179	6153416	0.6	00/30	11.86	67.80	A/B
					30/60	12.89	113.40	B2
2.24	580	313200	6153418	1.25	00/30	5.92	N/A	A
					30/60	14.52	88.90	B2
					60/90	13.69	108.10	B2
					90/125	13.67	129.50	B2/R

Site 3: Canham Road								
3.01	320	314285	6153745	0.65	00/30	1.40	31.50	A
					30/65	3.03	36.60	C/R

3.02	300	314268	6153749	0.5	00/30	2.37	44.80	A/B
					30/50	2.05	40.90	B/R
3.03	280	314247	6153750	0.55	00/30	0.98	44.50	A/B
					30/55	1.94	40.90	B/R
3.04	260	314228	6153748	0.4	00/40	1.05	62.50	A
3.05	240	314209	6153746	0.65	00/30	1.42	55.30	B
					30/65	1.28	36.30	R
3.06	220	314190	6153746	2.9	00/30	1.55	37.60	A/B
					30/60	2.84	30.80	B
					60/90	12.06	36.40	B2
					90/120	12.62	56.60	B2
					120/150	14.86	71.20	B2
					150/200	16.88	89.40	B2
					200/250	17.15	100.60	B2
					250/290	15.00	110.60	B2/R
3.07	200	314169	6153746	1.6	00/30	0.95	33.10	
					30/60	19.01	73.50	
					60/90	17.06	65.50	
					90/120	16.12	67.80	
					120-160	17.09	93.60	
3.08	180	314149	6153746	3.1	00/30	9.03	54.00	A/B
					30/60	15.54	45.20	B
					60/90	9.13	44.90	B
					90/120	15.48	50.10	B
					120/150	15.08	51.30	B
					150/200	14.48	55.30	B
					200/250	13.54	63.90	B

					250/310	10.97	65.60	B/R
3.09	160	314131	6153744	2.9	00/30	15.79	66.00	B2
					30/60	16.02	37.30	B2
					60/90	10.90	37.50	B2
					90/120	15.96	44.30	B2
					120/150	14.64	50.50	B2
					150/200	16.01	63.00	B2
					200/250	15.93	74.40	B2
					250/290	12.55	204.80	B2/R
3.1	140	314114	6153745	1.7	00/30	5.54	59.70	B2
					30/60	14.82	N/A	B2
					60/90	14.10	45.00	B2
					90/120	11.40	47.70	C
					120/150	7.10	58.00	C
					150/170	5.11	64.20	R
3.11	120	314092	6153741	4.2	00/30	2.79	50.70	A1
					30/60	11.02	51.90	B1
					60/90	10.60	43.20	B2
					90/120	8.05	37.20	B2
					120/150	4.81	38.20	C
					150/200	7.51	44.80	C
					200/250	5.02	45.20	C
					250/300	8.12	65.10	C
					300/350	5.01	31.60	C
					350/400	4.09	29.10	C
					400/420	4.29	40.50	C
3.12	100	314073	6153741	1.5	00/30	4.65	60.70	A/B

					30/60	11.00	40.70	B
					60/90	9.70	40.90	B
					90/120	6.76	38.60	C
					120/150	6.80	46.00	C
3.13	80	314054	6153739	3.3	00/30	2.84	59.00	A
					30/60	14.16	93.60	B2
					60/90	11.55	79.40	B2
					90/120	9.51	91.30	B2
					120/150	8.14	134.90	C
					150/200	7.71	199.20	C
					200/250	N/A	N/A	C
					250/300	7.01	232.20	C
					300/330	6.94	205.50	C
3.14	60	314031	6153740	2	00/30	4.86	67.60	A1
					30/60	5.00	40.70	A2/B
					60/90	16.71	59.20	B2
					90/120	12.53	56.80	B2
					120/150	11.99	103.80	C
					150/200	11.42	310.00	C
3.15	40	314014	6153741	1.8	00/30	6.30	72.30	A
					30/60	5.57	34.60	A2
					60/90	14.01	67.90	B2
					90/120	9.13	67.70	B2
					120/150	12.45	105.50	C
					150/180	10.11	158.00	C
3.16	20	313994	6153737	6.8	00/30	16.81	67.00	A/B
					30/60	16.56	50.60	B

					60/90	12.36	37.20	B/C
					90/120	9.99	34.70	C
					120/150	8.43	35.30	C
					150/200	7.93	37.10	C
					200/250	6.90	39.60	C
					250/300	9.21	78.50	C
					300/350	8.78	141.40	C
					350/400	10.01	307.00	C
					400/450	10.78	404.00	C
					450/500	14.59	366.00	C
					500/550	15.14	387.00	C
					550/600	17.13	519.00	C
					600/650	20.01	682.00	C
					650/680	17.63	602.00	C
3.17	0	313973	6153736	3.1	00/30	9.71	55.00	B
					30/60	6.96	38.90	C
					60/90	5.22	36.50	C
					90/120	6.27	35.00	C
					120/150	5.91	37.20	C
					150/200	4.72	36.40	C
					200/250	6.32	39.60	C
					250/300	7.99	53.70	C
					300/310	8.21	61.00	R

APPENDIX C:

GPR RADARGRAMS FOR SITE 1

All GPR data can be made available electronically upon request to the author.

Raw data is presented in greyscale. Processed data is presented in colour.

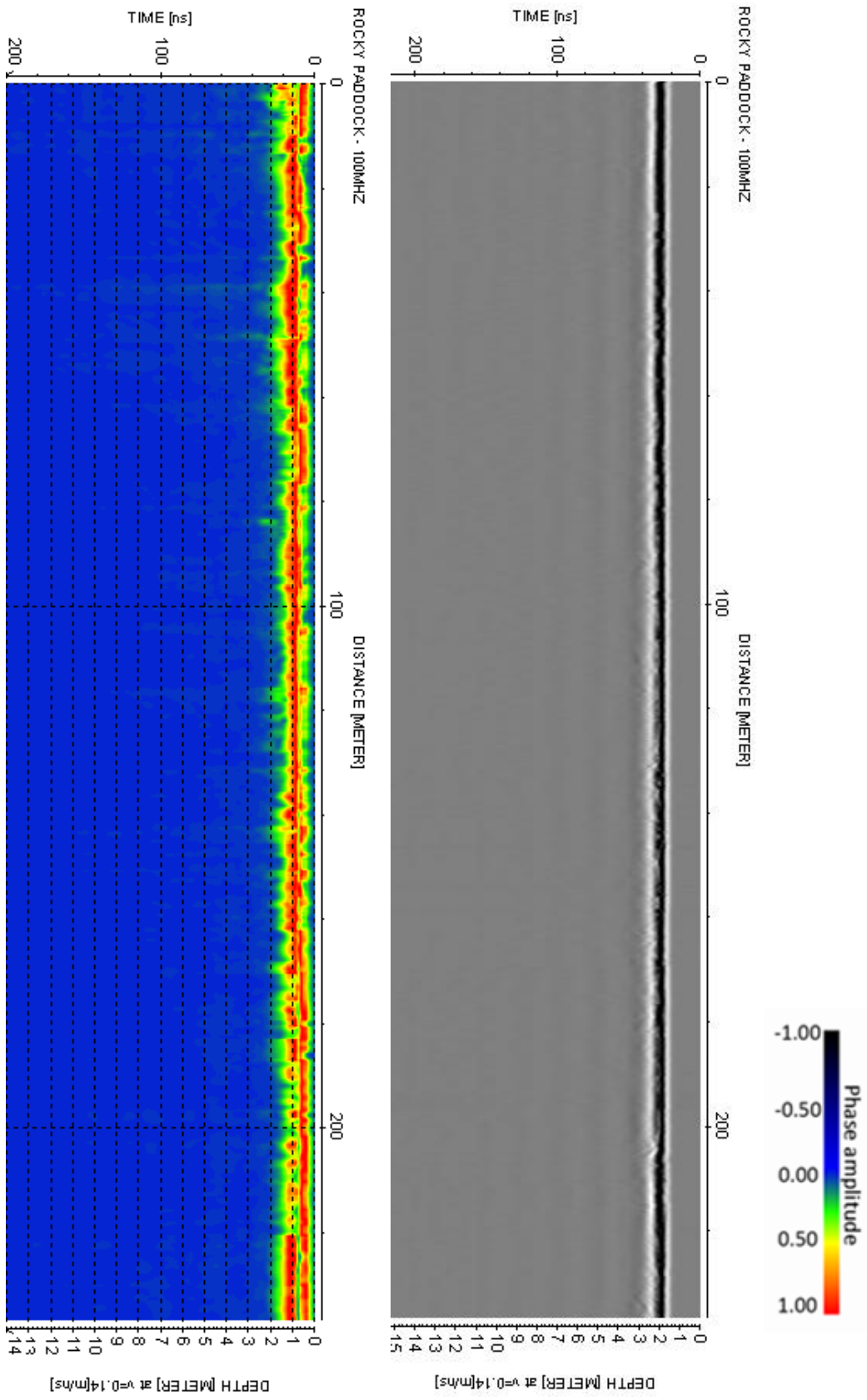

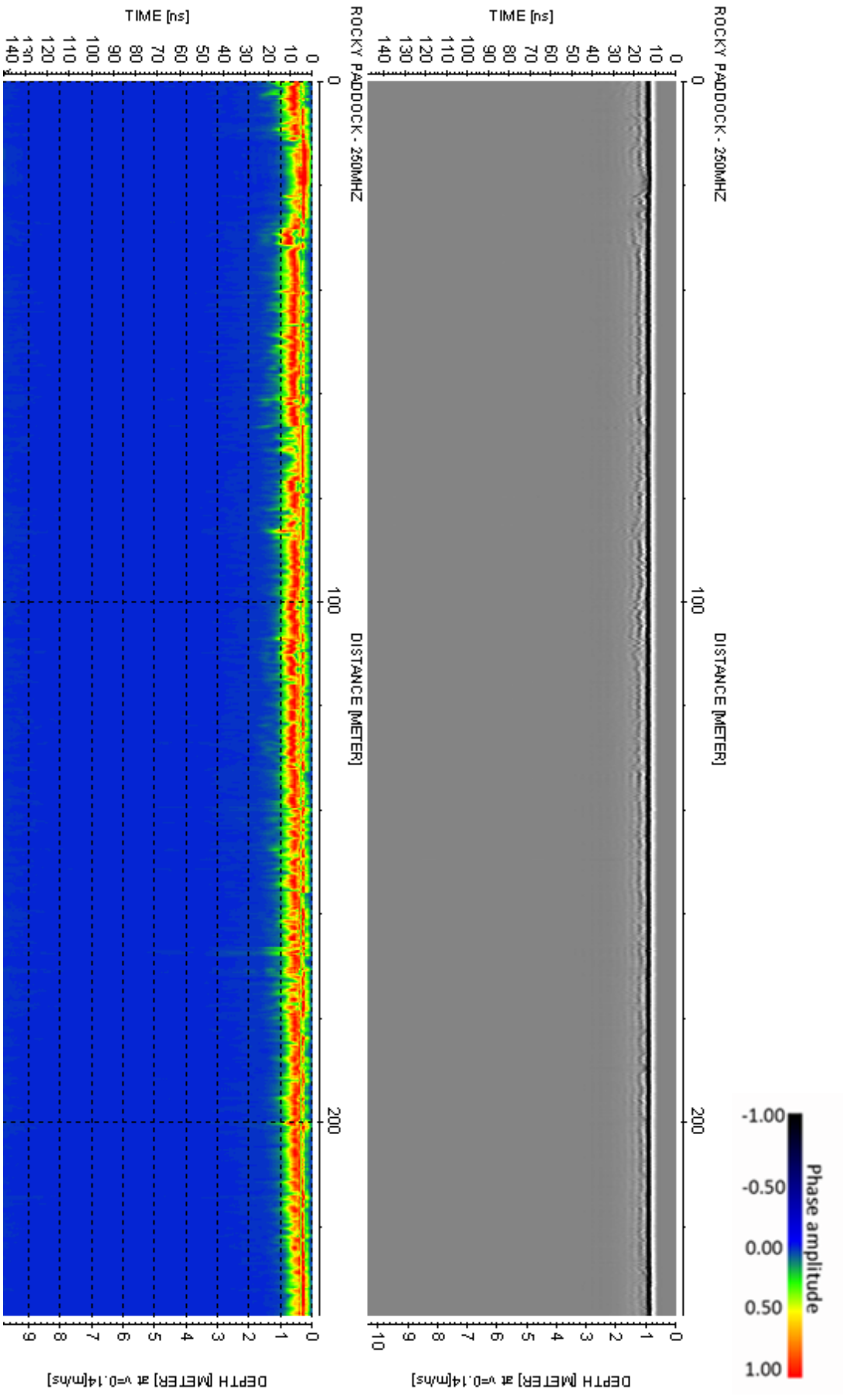
ROCKY PADDOCK - 250MHZ
TIME [ns]
DISTANCE [METER]
DEPTH [METER] at v=0.14[m/ns]
ROCKY PADDOCK - 250MHZ
TIME [ns]
DISTANCE [METER]
DEPTH [METER] at v=0.14[m/ns]
Phase amplitude
-1.00
-0.50
0.00
0.50
1.00

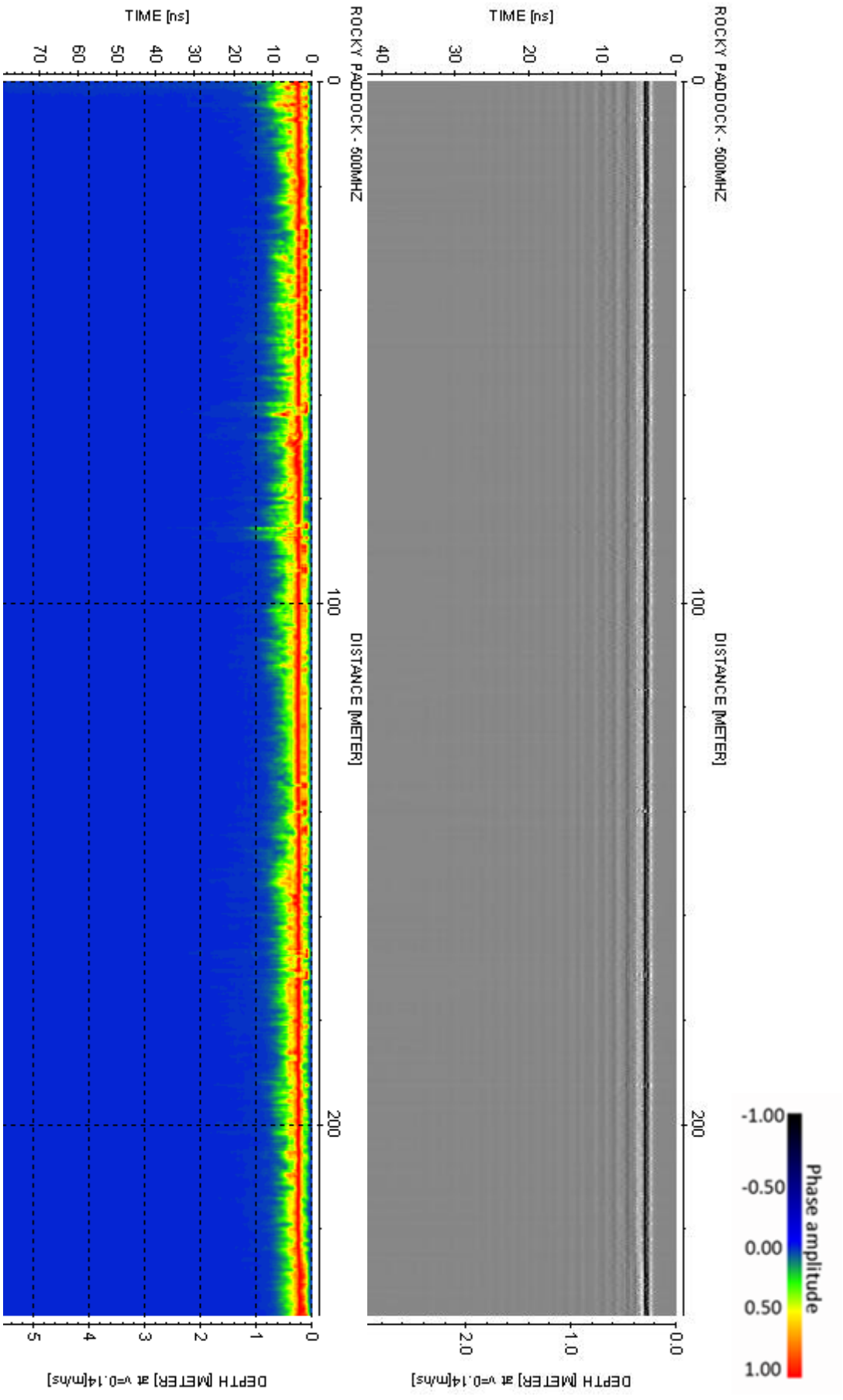
ROCKY PADDOCK - 500MHZ
TIME [ns]
DISTANCE [METER]
DEPTH [METER] at v=0.14[m/ns]
Phase amplitude
-1.00
-0.50
0.00
0.50
1.00

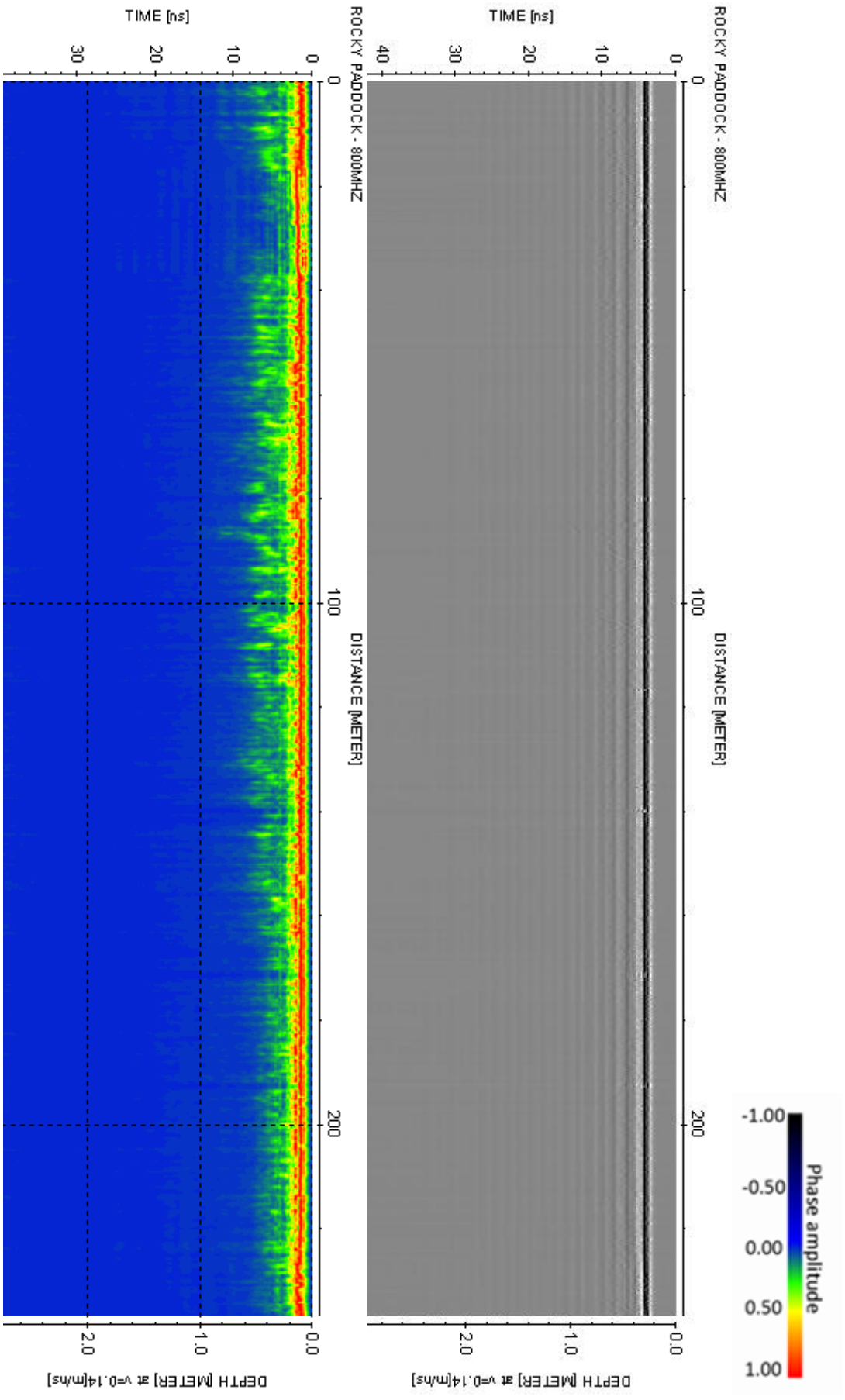
ROCKY PADDOCK - 800MHZ
TIME [ns]
DISTANCE [METER]
DEPTH [METER] at v=0.14[m/ns]
Phase amplitude
-1.00
-0.50
0.00
0.50
1.00

APPENDIX D:

GPR RADARGRAMS FOR SITE 2

Raw data is presented in greyscale. Processed data is presented in colour.

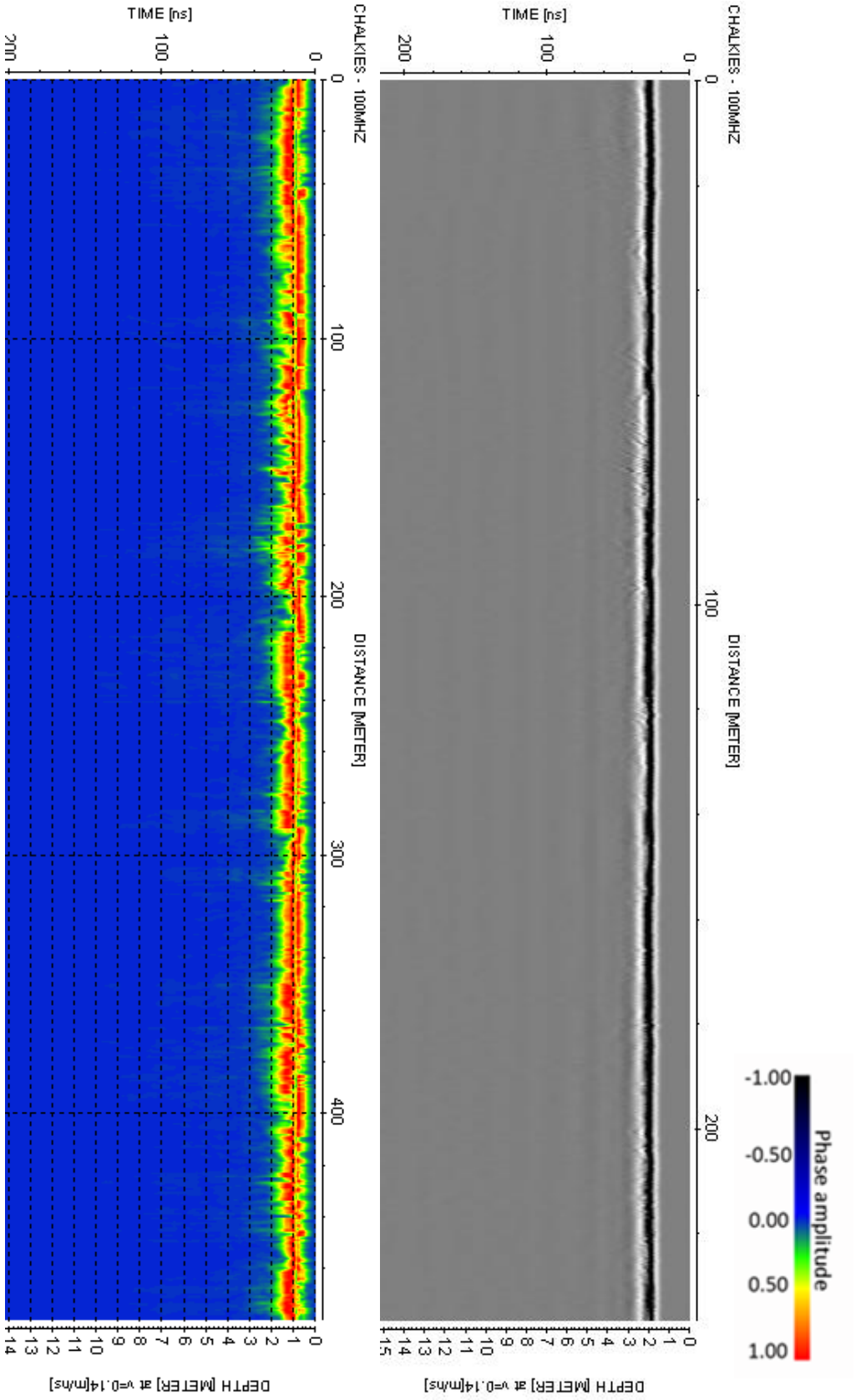

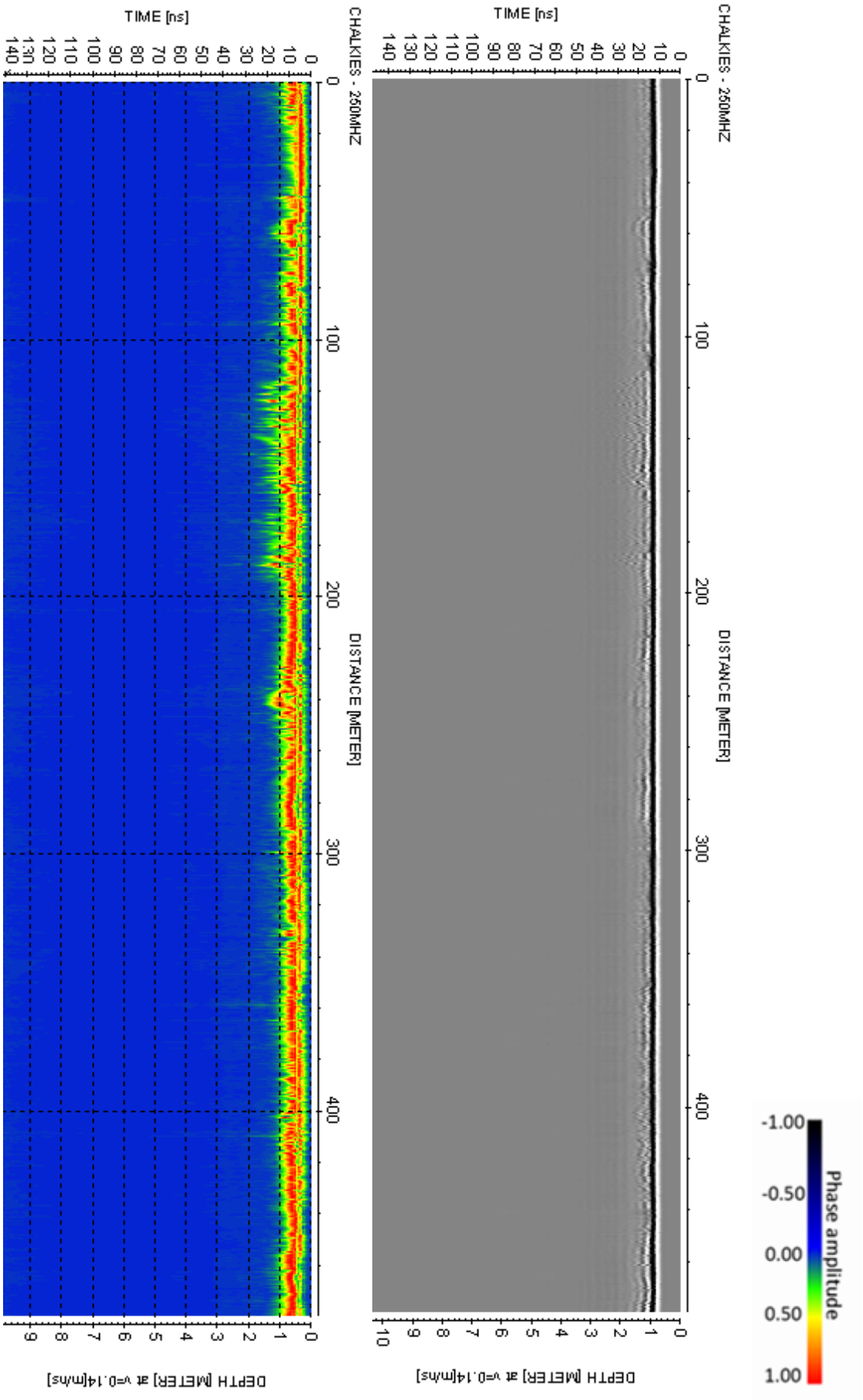
CHALKIES - 250MHZ
TIME [ns]
DISTANCE [METER]
DEPTH [METER] at v=0.14[m/ns]
CHALKIES - 250MHZ
TIME [ns]
DISTANCE [METER]
DEPTH [METER] at v=0.14[m/ns]
Phase amplitude
-1.00
-0.50
0.00
0.50
1.00

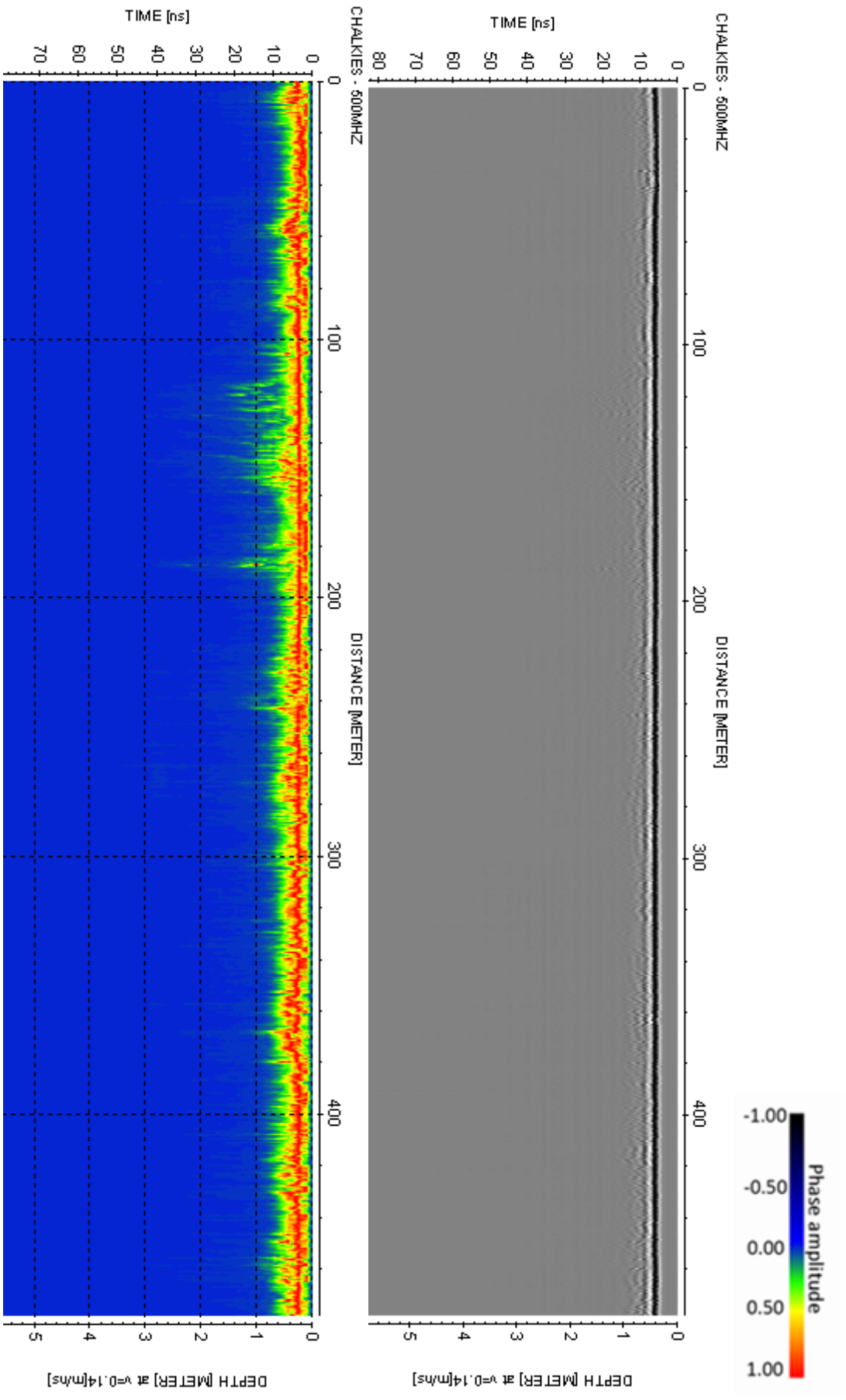
CHALKIES - 500MHZ
TIME [ns]
DISTANCE [METER]
DEPTH [METER] at v=0.14[m/ns]
Phase amplitude
-1.00
-0.50
0.00
0.50
1.00

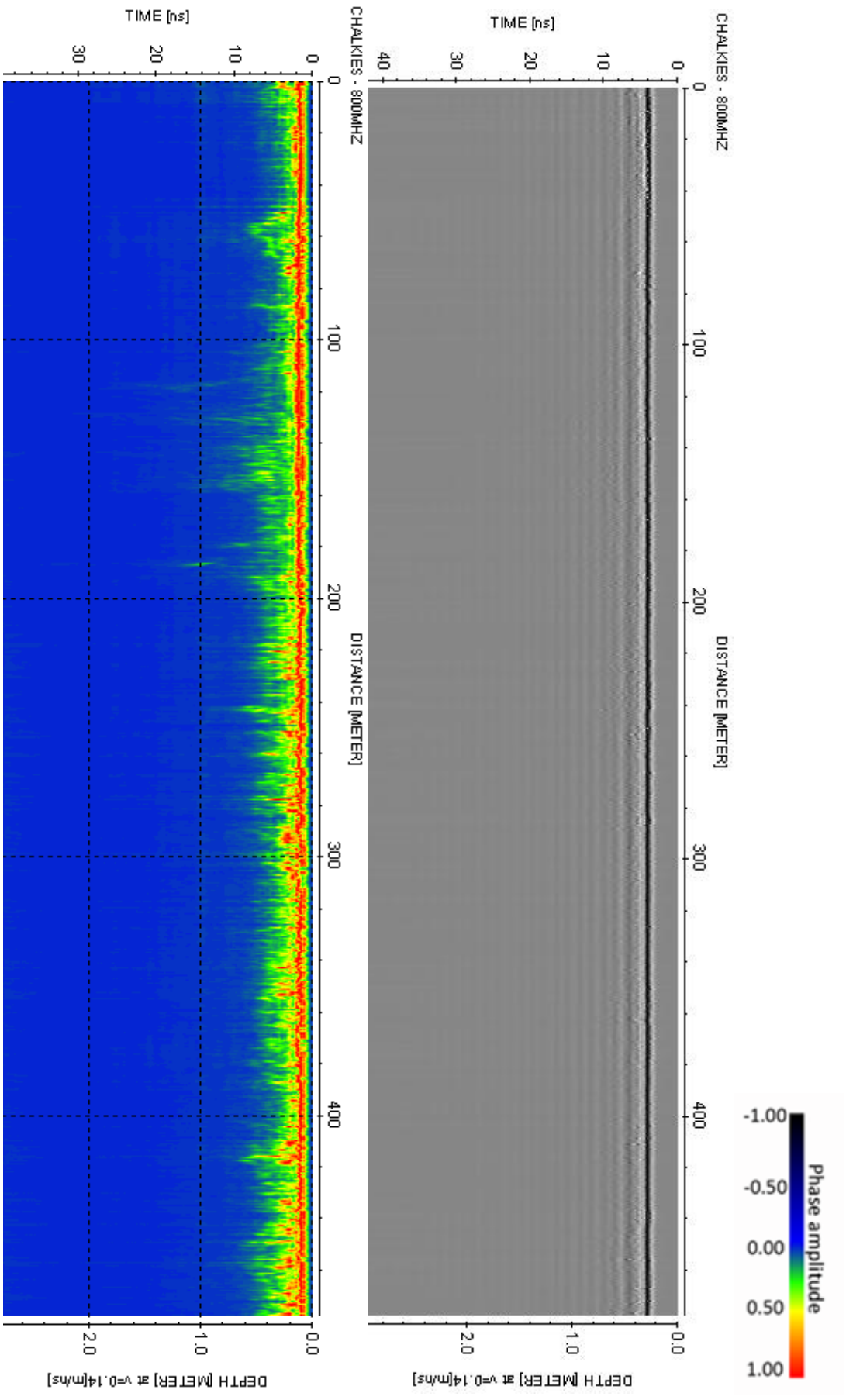
CHALKIES - 800MHZ
TIME [ns]
DISTANCE [METER]
DEPTH [METER] at v=0.14[m/ns]
Phase amplitude
-1.00
-0.50
0.00
0.50
1.00

APPENDIX E:

GPR RADARGRAMS FOR SITE 3

Raw data is presented in greyscale. Processed data is presented in colour.

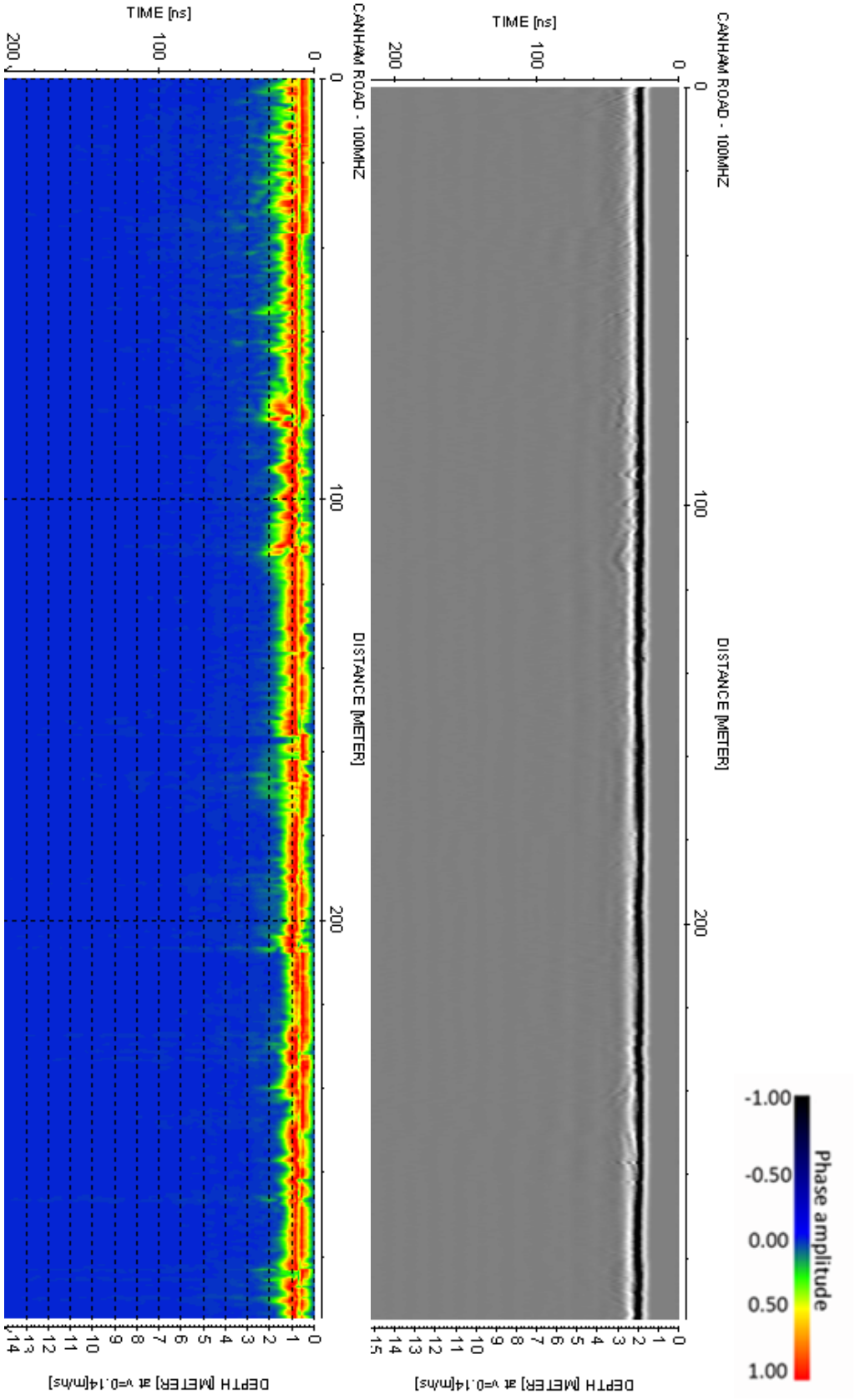

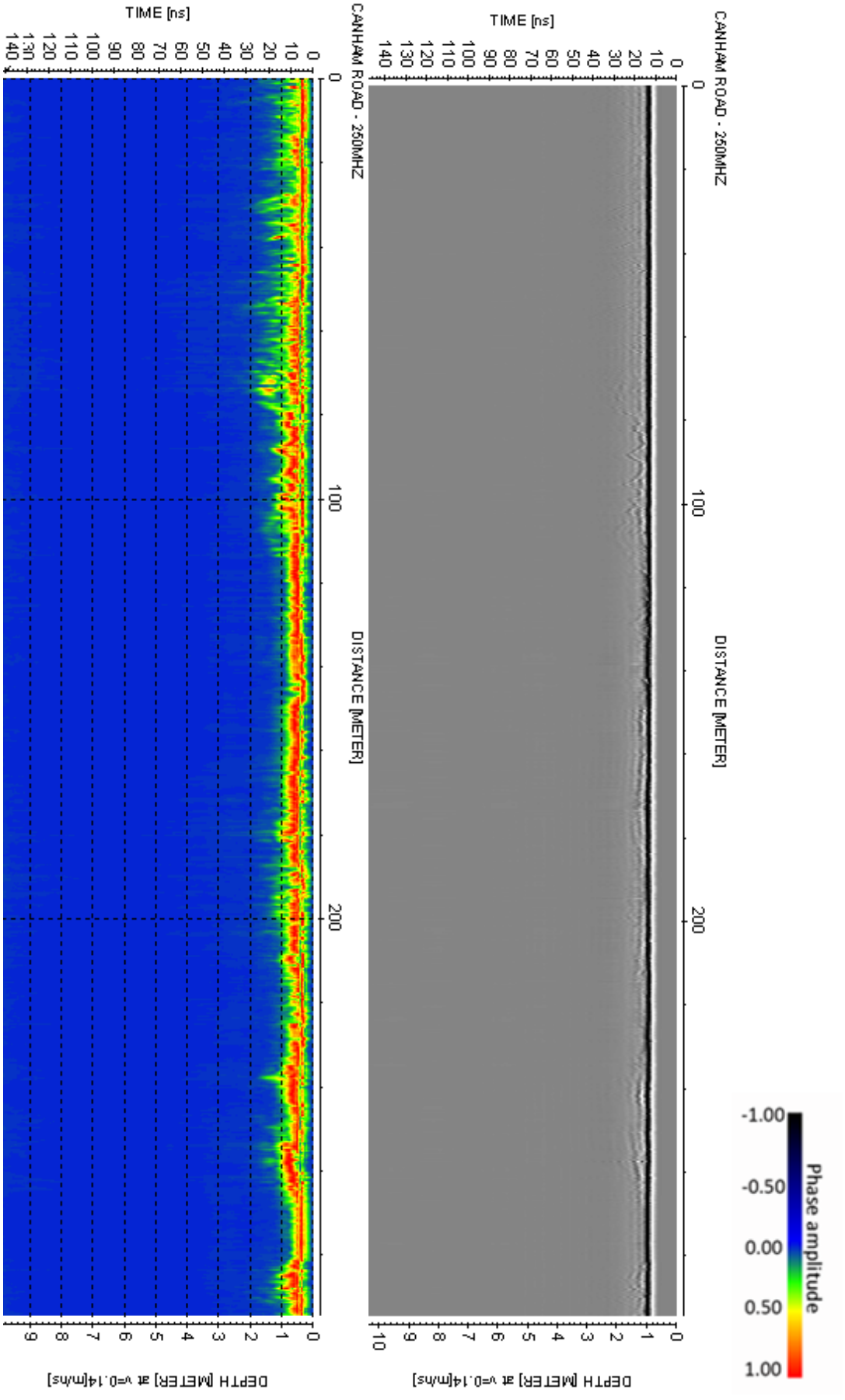
CANHAM ROAD - 250MHZ
TIME [ns]
DISTANCE [METER]
DEPTH [METER] at v=0.14[m/ns]
Phase amplitude
-1.00
-0.50
0.00
0.50
1.00

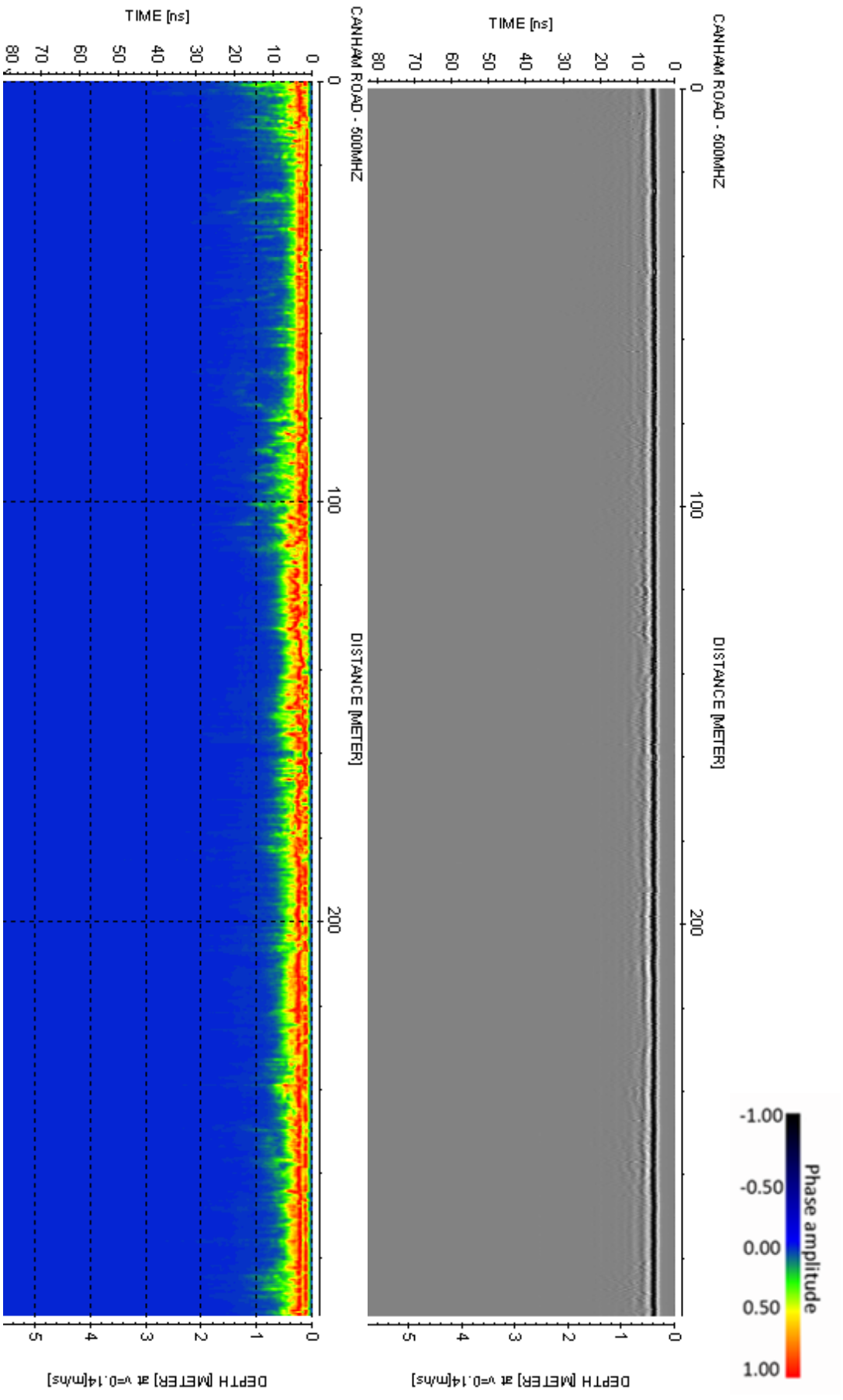
CANHAM ROAD - 500MHZ
TIME [ns]
DISTANCE [METER]
DEPTH [METER] at v=0.14[m/ns]
CANHAM ROAD - 500MHZ
TIME [ns]
DISTANCE [METER]
DEPTH [METER] at v=0.14[m/ns]
Phase amplitude
-1.00
-0.50
0.00
0.50
1.00

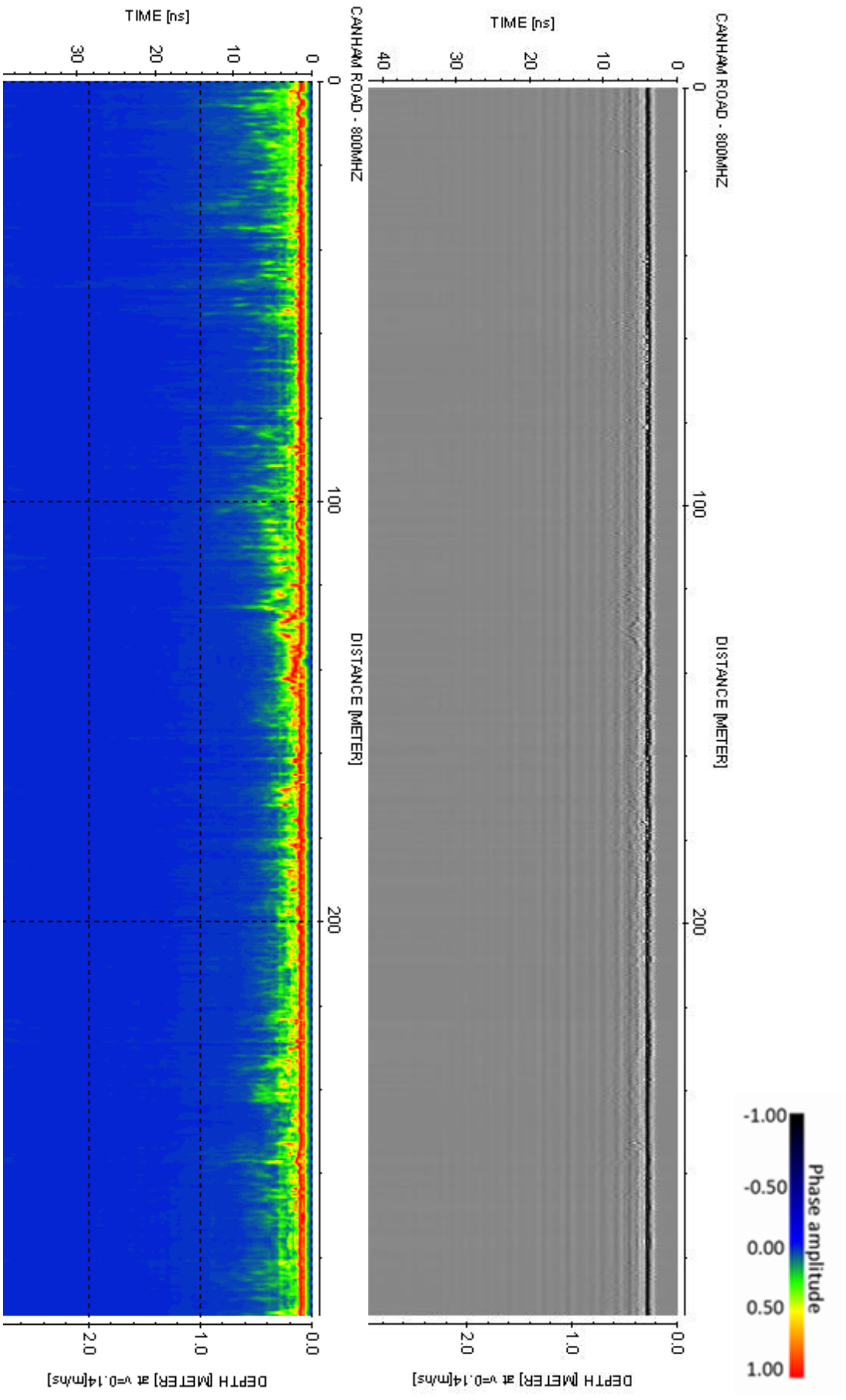
CANHAM ROAD - 800MHZ
TIME [ns]
DISTANCE [METER]
DEPTH [METER] at v=0.14[m/ns]
Phase amplitude
-1.00
-0.50
0.00
0.50
1.00